Annual Report to

Using Single-Molecule Imaging System Combined with Nano-fluidic Chip to Understand Fluid Flow in Tight and Shale Gas Formation

Project Number: 09122-29

Feb. 19, 2012

PI: Dr. Baojun Bai (baib@mst.edu)

Completed by Baojun Bai, Xiaolong Yin, Yinfa Ma, Keith Neeves, Yongpeng Sun, Jeong Tae Ok, Qihua Wu, Feng Xiao, Malek Elgmati

161 McNutt Hall, 1400 N. Bishop Ave.
Rolla, MO 65409

Tel: 573-341-4016

http://web.mst.edu/~baib

LEGAL NOTICE

This report was prepared by Baojun Bai et al as an account of work sponsored by
the Research Partnership to Secure Energy for America (RPSEA). Neither RPSEA, members of RPSEA, the National Energy Technology Laboratory, the U.S. Department of Energy, nor any person acting on behalf of any of these entities:

a. MAKES ANY WARRANTY OR REPRESENTATION, EXPRESS OR IMPLIED WITH RESPECT TO ACCURACY, COMPLETENESS, OR USEFULNESS OF THE INFORMATION CONTAINED IN THIS DOCUMENT, OR THAT THE USE OF ANY INFORMATION, APPARATUS, METHOD, OR PROCESS DISCLOSED IN THIS DOCUMENT MAY NOT INFRINGE PRIVATELY OWNED RIGHTS, OR

b. ASSUMES ANY LIABILITY WITH RESPECT TO THE USE OF, OR FOR ANY AND ALL DAMAGES RESULTING FROM THE USE OF, ANY INFORMATION, APPARATUS, METHOD, OR PROCESS DISCLOSED IN THIS DOCUMENT.

THIS IS A FINAL REPORT. THE DATA, CALCULATIONS, INFORMATION, CONCLUSIONS, AND/OR RECOMMENDATIONS REPORTED HEREIN ARE THE PROPERTY OF THE U.S. DEPARTMENT OF ENERGY.

REFERENCE TO TRADE NAMES OR SPECIFIC COMMERCIAL PRODUCTS, COMMODITIES, OR SERVICES IN THIS REPORT DOES NOT REPRESENT OR CONSTIITUTE AND ENDORSEMENT, RECOMMENDATION, OR FAVORING BY RPSEA OR ITS CONTRACTORS OF THE SPECIFIC COMMERCIAL PRODUCT, COMMODITY, OR SERVICE.

Blank page

Signature page

Baojun Bai, Principal Investigator

Date

ABSTRACT

Tight sand and shale gas exist in underground reservoirs with a micro-Darcy (μD) range of permeability and are characterized by nanosized pore throats and crack-like interconnections between pores. The flow of gas and introduced fluid, such as hydraulic fracturing fluid, in these fractures is not well understood. The current study will help to address this problem.

A fluidic chip consisting of two micro-scale channels connected by a series of parallel nano-scale channels is fabricated with silicon and Pyrex. The chip can withstand pressures of up to 1000 psi and temperatures of up to 100°C. Its transparent matrix enables the direct observation of immiscible fluids interacting on the nano-scale. Single- and two-phase flow experiments are conducted in micro-fabricated porous media analogs (PMA) with random homogeneous and heterogeneous networks based on Voronoi tessellations.

The additives in fracturing fluids may impair fracture permeability and alter rock wettability, thus influencing gas flow. To remedy this problem, intensive studies of rock surface and fluid composition interaction are performed in order to better understand the impact of induced fluid on rock surface wettability. The mineralogy of gas shale samples are analyzed using x-ray diffraction in an effort to reveal any relationship between mineralogy and wettability. Contact angle measurements are performed, and the effect of various fracturing fluid additives on wettability are examined.

The single-molecule detection apparatus used in the biosciences is modified to study the gas liquid flow behavior in nano-chips. This system can measure physical parameters as well as chemical/biochemical reactions and interactions because the data are obtained in real time rather than by averaging. Using the single-molecule imaging system, the flow behaviors of natural gas and introduced fluids (water, surfactant solutions and polymers) in capillary models that mimic micro-fractures existing in shale gas formations are investigated. Different models with various geometries and wettability conditions are used for these tests.

A three-dimensional, parallelized, multi-fluid lattice Boltzmann simulator is developed. This simulator can use real porous media images obtained from micro-computed tomography (micro-CT) or a focused ion beam (FIB)–scanning electronic microscope (SEM) as input parameters. The simulator also can employ synthetic geometry models. Results obtained from single-phase flow simulations agree well with existing and new experimental and numerical data.

TABLE OF CONTENTS

ABSTRACT v
TABLE OF CONTENTS vi
LIST OF FIGURES viii
LIST OF TABLES x
EXECUTIVE SUMMARY 1
1. Nano-fluidic chip construction 3
1.1 Introduction 3
1.2 Experimental Method 4
1.3 Results and Discussions 5
1.4 Conclusions and Future Work 9
2. Wettability tests to understand the interaction between hydraulic fluid compositions and rocks in macroscale 10
2.1 Introduction 10
2.2 Experimental Methods 10
2.2.1 Materials 10
2.2.2 Equipment 14
2.3 Results and Discussions 16
2.3.1 X-Ray Diffraction and Clay Mineralogy 16
2.3.2 Contact angle 19
2.4. Conclusions 21
2.5 Future work 21
2.5.1 Imbibition method 22
2.5.2 Membrane permeability measurement 23
3. Nano-fluidic chip experiments to understand fluid flow on nano-scale pore spaces and cracks 24
Part I. Liquid flow behavior in micro-scale channels that mimic micro-fractures in shale gas formation 24
3.1 Introduction 24
3.2 Experimental methods 24
3.2.1 Materials 24
3.2.2 Micro-/Nano-model preparation 25
3.2.3 Experimental setup 25
3.2.4 Characterization of the wettability conditions and sizes of modified micro-channels 27

3.2.5 Experimental procedure 27
3.3 Result and discussion 28
3.3.1 Experimental setup optimization 28
3.3.2 Polymer/decane fluid flow behavior in micro-models 28
3.3.3 Effect of channel size and wettability on the flow behavior of polymer particles 33
3.4 Future work 38
3.5 Conclusions 38
Part II. Gas/fluid flow behavior in the nano-channels 39
3.6 Experimental method 39
3.7 Future experimental plan 41
3.8 Review: Published study of gas flow behavior in micro-/nano-channels 42
4. Numerical simulation 45
4.1 Introduction 45
4.2 Methods 45
4.3 Results and Discussions 51
4.4 Conclusions and Future Work 54
5. Technology Transfer Efforts 55
5.1 Project Website 55
5.2 Presentations 55
5.3 Posters 55
5.4 Full papers 55
REFERENCES 57
LIST OF ACRONYMS AND ABBREVIATIONS 59

LIST OF FIGURES

Figure 1-1: Cross-sectional schematic of Si-Pyrex micro- and nano-channel fabrication process 4

Figure 1-2: (a) – (d) Electron micrographs of nano-fluidics chips. 5

Figure 1-3: Permeability of (A) homogeneous and (B) heterogeneous networks 6

Figure 1-4: Displacement of oil (gray fluid) by water (black fluid) as a function of network topology and wetting. 8

Figure 2-1: Stratigraphy and Location Map of the Haynesville Shale [3] 11

Figure 2-2: Utica Shale Gas Play Geographic and Cross-Section Map [8] 12

Figure 2-3: Stratigraphy and Location Map of the Fayetteville Shale [3] 13

Figure 2-4: Equilibrium of Forces at Liquid-Vapor-Solid Interface 15

Figure 2-5: Contact Angle Goniometer Instrument 16

Figure 2-6: X-ray diffraction results of the five shale gas samples. 18

Figure 2-7: Contact angle results of the five shale gas samples using six fracturing fluid additives. 19

Figure 2-8: Flowchart of wettability alteration evaluation 22

Figure 2-9: Schematic of imbibition setup 23

Figure 3-1: Optical arrangement for single-molecule detection system 26

Figure 3-2: Localized probing region of single-molecule imaging system 26

Figure 3-3: Experimental setup: Fluid transfer system 26

Figure 3-4: Initial pressure vs. time with different capillary lengths (capillary ID = 100μm, flow rate = 1.0ml/h) 29

Figure 3-6: Initial pressure vs. time with water compared to polymer solution (friction reducer) (capillary ID = 100μm, flow rate = 1.0ml/h) 30

Figure 3-7: Initial pressure vs. time with different wettability channels (capillary ID = 100μm, flow rate = 1.0ml/h) 30

Figure 3-11: Mobility of interfaces with different sizes of capillary tubes (capillary length = 10cm, 0.1%FRW-18) 33

Figure 3-12: Shape of the interfaces: (a) 100um ID capillary, 20x lens, decane push 0.1%FRW-18, d= 5cm ; (b) 100um ID capillary, 20x lens, lab reagent water push 0.1%FRW-18, d= 5cm 33

Figure 3-13: Hydrophilic (a) and hydrophobic (b) inner surface micro-channels 34

Figure 3-14: Meniscus heights of water in unmodified and modified micro-channels. 34

Figure 3-15: (a) Images of polymer particle FRW-20 (b) Size distribution of polymer particles (FRW-20, 0.1% v/v) 35
Figure 3-16: Aggregation configuration of FRW-20 under different micro-channel wettability conditions and sizes 36
Figure 3-17: Focusing plane 36
Figure 3-18: The average velocity distribution of FRW-20 in different positions along the Y-axis in micro-channels with different sizes and wettability conditions. 37
Figure 3-19: The average velocity distribution of FRW-20 in different positions along the Y-axis in micro-channels with different sizes and wettability conditions 38
Figure 3-20: Schematic of experimental setup 39
Figure 3-22: Image of the channels of the nano-chips (main channel and nano-channels) 41
Figure 3-23: Schematic of epi-fluorescence system for molecular tagging velocimetry method 42
Figure 4-1: Generation of a fully-percolated pore network from a 2D Voronoi diagram 46
Figure 4-2: Synthetic porous media geometries for flow simulations. 47
Figure 4-3: Flow diagram of three-dimensional, parallelized lattice Boltzmann multi-fluid simulator. 51
Figure 4-4: Parallel speedup of 3D single-phase lattice Boltzmann simulator 52
Figure 4-5: Porosity-permeability relation of idealized synthetic geometries established from single-phase lattice Boltzmann simulations. 52
Figure 4-6: Two-fluid test conducted using the Shan-Chen model [9, 10]. 53

LIST OF TABLES

Table 2-1: Examined gas shale sample data 11
Table 2-2: Basal Spacing (d) in Å and 2θ for Cu K-Alpha Radiation* 17
Table 2-3: Summary of Qualitative XRD Results 18
Table 2-4: Contact Angle Results Summary* 20
Table 3-1: Basic information of FRW-20 25
Table 3-2: Basic information of fluorescein for polymer labeling 25
Table 3-3: Experimental conditions 27
Table 4-1: Parameters in the Shan-Chen model [3, 4] and their physical meanings. 53

EXECUTIVE SUMMARY

This project focuses on clarifying the flow behavior of natural gas and introduced fluids (water, surfactant solutions and polymers) in micro-fractures and nano-sized pores of tight gas and shale formations by using an advanced single-molecule imaging system combined with nano-fluidic chips and pore-scale numerical simulation techniques.

Using the advanced nano-fabrication techniques originally developed in the semiconductor industry, we have developed a novel pore-scale model to investigate multiphase flows. This model contains 5 μm wide, 100 nm deep channels etched on silicon and then covered by Pyrex. This nano-fluidic device, which allows direct observation of the interaction between two immiscible fluids on the nano-scale, can withstand pressures of up to 1,000 psi and temperatures of up to 100 °C. This device will be used to visualize gas-liquid relative movement on the nano-scale in the next reporting year.

An XRD mineralogy analysis and contact angle measurement were conducted on various shale samples. The XRD analyses provided insight into clay and non-clay mineralogy, showing high illite content in the Haynesville and Utica shale samples. It also suggested high calcium carbonate (lime) content in the Utica shale samples. Calcite content is the dominate factor in increasing the gas shale contact angle and changing the wettability of gas shale rock to oil-wet. Organic matter content governed the wettability alterations of calcareous samples. In order to characterize the shale/tight sand wettability alteration condition, an imbibition setup is proposed, which would be combined with the membrane permeability setup in future work. This would facilitate understanding of the wettability alteration during hydraulic stimulation treatment.

The flow behaviors of polymer/decane fluids in different capillary models that mimic micro-fractures were monitored using a single-molecule imaging system. We studied the effect of channel dimensions and wettability on the flow and aggregation behavior of polymer particles in micro-scale channels. Flow velocity distribution and aggregation configuration were characterized. The setup of the experiment then was optimized in order for the nano-chips to apply to the study's purpose. Preliminary tests were conducted with the nano-chips, and the experimental setup and gas/introduced fluid flow characterization will be investigated next. Gas visualization will be achieved as well using the molecular tagging velocimetry method with the optimized epifluorescence system.

A three-dimensional, parallelized lattice Boltzmann fluid flow simulator was developed. This simulator demonstrates a nearly ideal speedup. As test problems, the porosity-permeability relationships in three synthetic porous media geometry types (fractured, tubular and fibrous) were studied. The results agree well with published data. A direct comparison with experiments conducted in micro-fluidic networks also showed excellent agreement. Our implementation of multiple fluids

successfully reproduced the interfacial tension and contact angle under different wetting conditions.

1. Nano-fluidic chip construction

1.1 Introduction

The objective of this task (Task 4) is to fabricate nano-fluidic chips to enable the study of multiphase flow on a length scale more relevant to the size of pores in tight gas and shale formations. Two milestones were identified for this task:

a) Fabrication of PDMS, silicon, and quartz micro-fluidic and nano-fluidic networks (End of Year 1);
b) Single- and two-phase flow experiments in micro-fluidic and nano-fluidic networks (End of Year 2).

We successfully met our Year 1 obligation by developing a fabrication scheme for nano-fluidics chips. The chips, fabricated in silicon and Pyrex, consist of two micro-scale channels connected by a series of parallel nano-scale channels. They are capable of withstanding pressures of up to 1000 psi and temperatures of up to 100°C. In the Experimental Method section, the details of the fabrication process are described briefly.

Single- and two-phase flow experiments were conducted in micro-fabricated porous media analogs (PMA). Most experimental porous media models consist of periodic geometries that lend themselves to comparison with well-developed theoretical predictions. However, many real porous media, such as geological formations, contain a degree of randomness and complexity at certain length scales that is not adequately represented in periodic geometries. To design an experimental tool to study these complex geometries, we created micro-fluidic models of random homogeneous and heterogeneous networks based on Voronoi tessellations. These networks consisted of approximately 600 grains separated by a highly connected network of channels with an overall porosity of 0.11–0.20. We found that introducing heterogeneities in the form of vugs within the network changed the permeability in a way that cannot be predicted by the classical porosity-permeability relationship known as the Kozeny equation. The permeability values found in our experiments agreed excellently with those calculated from three-dimensional lattice Boltzmann simulations. In two-phase flow experiments of oil displacement with water, we found that the wettability of channel walls determined the pattern of water invasion, while the network topology determined the residual oil saturation. The presence of vugs increased the microscopic sweeping efficiency in water-oil displacement. These results suggest that complex network topologies lead to fluid flow behavior that is difficult to predict based solely on porosity.

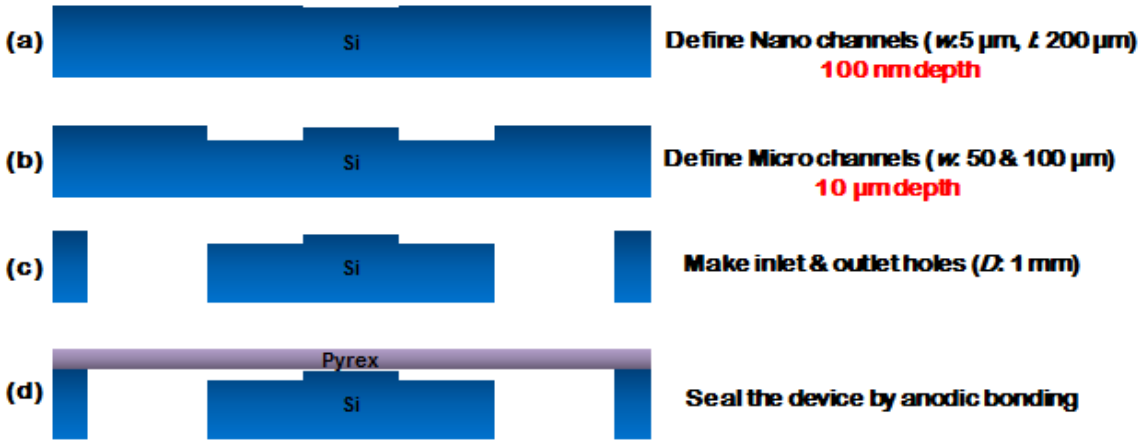

Figure 1-1: Cross-sectional schematic of Si-Pyrex micro- and nano-channel fabrication process

1.2 Experimental Method

Both micro- and nano-scale features were etched into silicon nitride-coated <100> silicon wafers using a combination of photolithography and reactive ion etching. Figure 1-1 shows the overall fabrication procedure of the nano-fluidic chips. First, a series of 100 parallel nano-channels were defined by photolithography, followed by CF_4 reactive ion etching (RIE) of the nitride and SF_6 REI of the silicon (Fig 1-2a). The channel width, as defined by photolithography, was 5 µm wide and 200 µm long. The channel depth, as defined by RIE, was 100 nm (Fig. 1-2c). This shallow silicon plasma etch provided nanometer control over the channel depth. The next step was etching micro-channels using a similar procedure. The major difference is that instead of the isotropic etch used to define nano-channel depth, we used an anisotropic etching technique known as the Bosch process, a two-step process of alternating etching and deposition steps. The end result is the ability to define straight sidewalls many microns in depth. Here, we etched two micro-channels perpendicular to the nano-channels to a depth of 10 µm. The final silicon processing step was a backside etch to define the inlet and outlet holes and release the device from the wafer. Again, we used the Bosch process to bore four holes (diameter = 1 mm) through the entire wafer (thickness = 0.5 mm) using a nitride etch mask. The final relief structure in the silicon wafer is shown in Figure 1-2. The scalloped side-wall profile (Figure 1-2d) is a result of the Bosch process. All silicon processing was performed at the Center for Nanophase Materials Science at Oak Ridge National Laboratory.

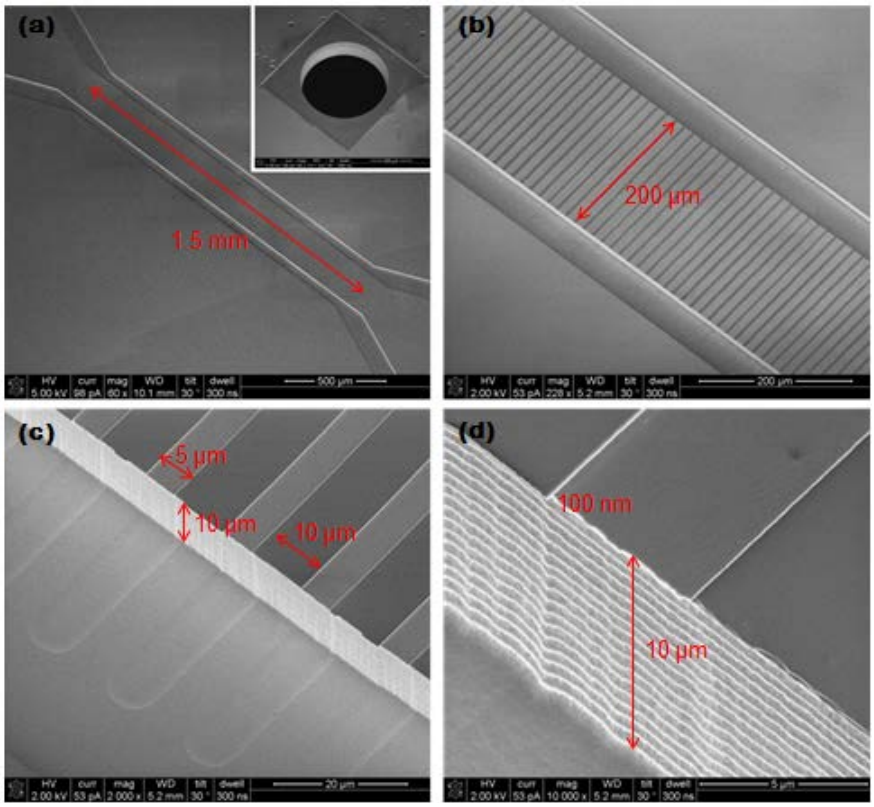

Figure 1-2: (a) – (d) Electron micrographs of nano-fluidics chips.

Silicon structures were transported back to CSM for cleaning and assembly. Photoresist etch masks were removed using wet (Piranha) and dry (oxygen plasma) etching. Silicon nitride etch masks were removed using phosphoric acid at 80 C. After a careful inspection of all features, the silicon devices were bonded to Pyrex coverslips using anodic bonding at 330 °C and 1 kV. The Pyrex top offers an optically transparent substrate for visualizing fluid flow and solute transport. Finally, PEEK Nanoports (Idex Health and Science) were bonded to the inlet and outlet holes by epoxy (rated to 1500 psi). Small bore PEEK or stainless steel tubing can be connected to the device through the Nanoports.

1.3 Results and Discussions

Fabrication of Nano-Fluidic Chips: The major technical challenge in this study was finding the right fabrication scheme and materials to meet the design specifications. Owing to the high pressures desired for gas-liquid experiments, we had to abandon the elastomer-based materials used in our previously developed micro- and nano-fluidics models. Therefore, we chose to use silicon as the primary structural element of our first prototype. Silicon is the most widely characterized material for nano-fabrication because it is the architecture upon which integrated circuits are built. Particularly relevant to this project is the existence of well-developed methods for anisotropic etching of silicon at the nano-scale, as outlined above in the Experimental Methods section. The drawback of silicon is that it is opaque and therefore not compatible with optical microscopy. To address this issue, we

introduced a transparent top to our silicon devices. The anodic bonding of Pyrex glass and silicon is commonly used for other single molecule fluorescence measurements, such as DNA visualization.

The final device allows for the observation of the interaction between two immiscible fluids. Each fluid is independently controlled through one of the two micro-channels (Fig. 1-2). The relatively wide channels (5 μm) with nano-scale depths of 100 nm provide a means by which to observe fluid interaction at the nano-scale. In our initial laboratory testing, we were able to visualize the gas-liquid meniscus within the nano-channels with bright field microscopy at 200X magnification.

Fluid Flow in Micro-fluidic Chips: Single-phase flow experiments were conducted in micro-fluidic PMA for both homogeneous and heterogeneous (vugs) networks (Fig. 1-3). The average permeability of the homogeneous networks was 0.42 ± 0.02 μm^2, with a range of 0.37 μm^2 to 0.43 μm^2. The low standard deviation and small range of permeabilities suggests that these random geometries were statistically similar and that the size of the network was sufficiently large to be a representative elementary volume.

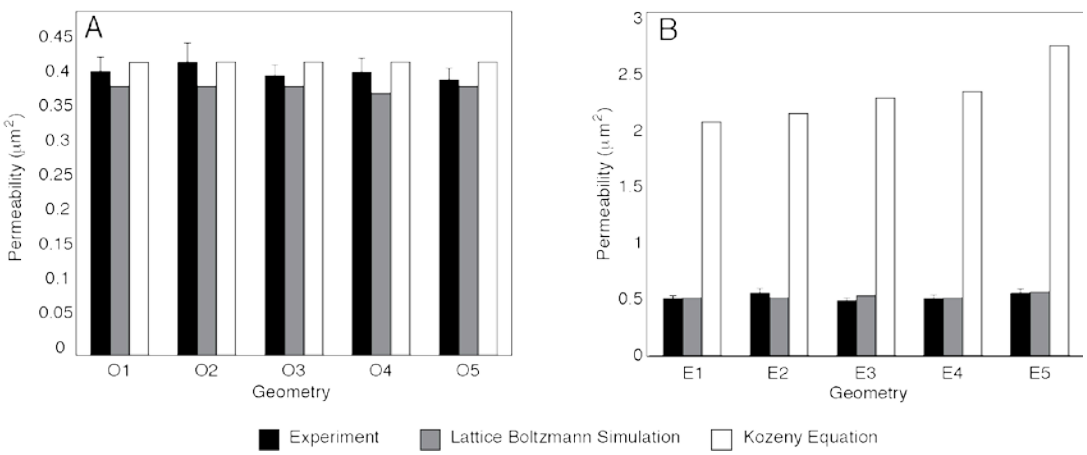

Figure 1-3: Permeability of (A) homogeneous and (B) heterogeneous networks

A completely homogenous network is a simplification that is rarely, if ever, encountered in real porous media. One source of heterogeneity is the contrast between cavities (pore bodies) and conduits (pore throats). The ratio between the size of the cavity and the size of the conduit is a measure of the level of microscopic heterogeneity. Extremely heterogeneous porous media often feature large cavities referred to as vugs. Vugs are caused by minerals dissolving within a sedimentary rock matrix and are predominately associated with carbonate rocks. Vugs may be O(100) times larger than the inter-vug connections. To study the effect of microscopic heterogeneity on fluid flow, single grains or clusters of grains were removed. When 10% of the grains were removed and the average cavity size was about sixteen times that of the conduits, a two-fold increase in porosity was observed. When the cavities consisted of clusters of grains and their sizes were

about 40-50 times that of conduits, the porosity after grain removal increased from 11% to about 19%. There was no significant difference in either the permeability gain or the absolute value of the average permeability between removing single grains (0.53 μm^2) or clusters of grains (0.55 μm^2). These data suggest that the total volume of the vugs, not their individual size, determines the increase in permeability compared to the homogenous networks. Using the electric circuit analogy, the resistance (inverse permeability) in the fluidic circuit will be determined by the largest resistors (channels), with a negligible contribution from the resistance through the vugs. In essence, the vugs simply remove some of the high-resistance channels from the network, leading to an overall increase in permeability.

The experimental permeability measurements can be compared to theoretical predictions using a porosity-permeability relationship. The most commonly-used relationship is the semi-empirical Kozeny equation. The Kozeny equation is a good predictor of permeability for the homogeneous networks, which is not surprising because these networks are physical realizations of the capillary tube model upon which the Kozeny equation was established. However, the Kozeny equation severely overestimates the permeability in heterogeneous networks by four- to five-fold. In our heterogeneous networks, the inclusion of vugs approximately doubles the porosity. Due to the cubic dependence on porosity, the Kozeny equation predicts an eight-fold increase in permeability with a doubling of the porosity. The experimentally measured permeability only increases by approximately 30% with the introduction of vugs. When the Kozeny equation is applied to the heterogeneous geometries, it interprets the porosity increase introduced by the vugs as more capillary tubes. However, because the vugs are isolated, their porosity does not increase the permeability as strongly as that in inter-connected capillaries, which causes the overprediction of the Kozeny equation.

A typical example of two-phase flow in porous media is the displacement of oil by an aqueous solution in secondary and tertiary oil recovery processes. We simulated this process with a corner-to-corner flow in both homogeneous and heterogeneous networks (Fig. 1-4). In homogeneous networks, oil was displaced in a smooth, continuous fashion until breakthrough for both hydrophilic and hydrophobic walls. However, the low resistance of the vugs in heterogeneous networks resulted in an interesting filling pattern. Prior to the water arriving at a vug, the water displaced the oil in a continuous manner similar to that seen in homogeneous networks. However, once the water arrived at the vug, the displacement in the rest of the network stopped until the entire vug was filled with water. After the vug was filled, normal displacement continued until the next vug was reached. The interpretation of this observation is that once the capillary pressure is overcome at the inlet of a vug, the vug becomes a high-permeability pathway into which water preferentially drains.

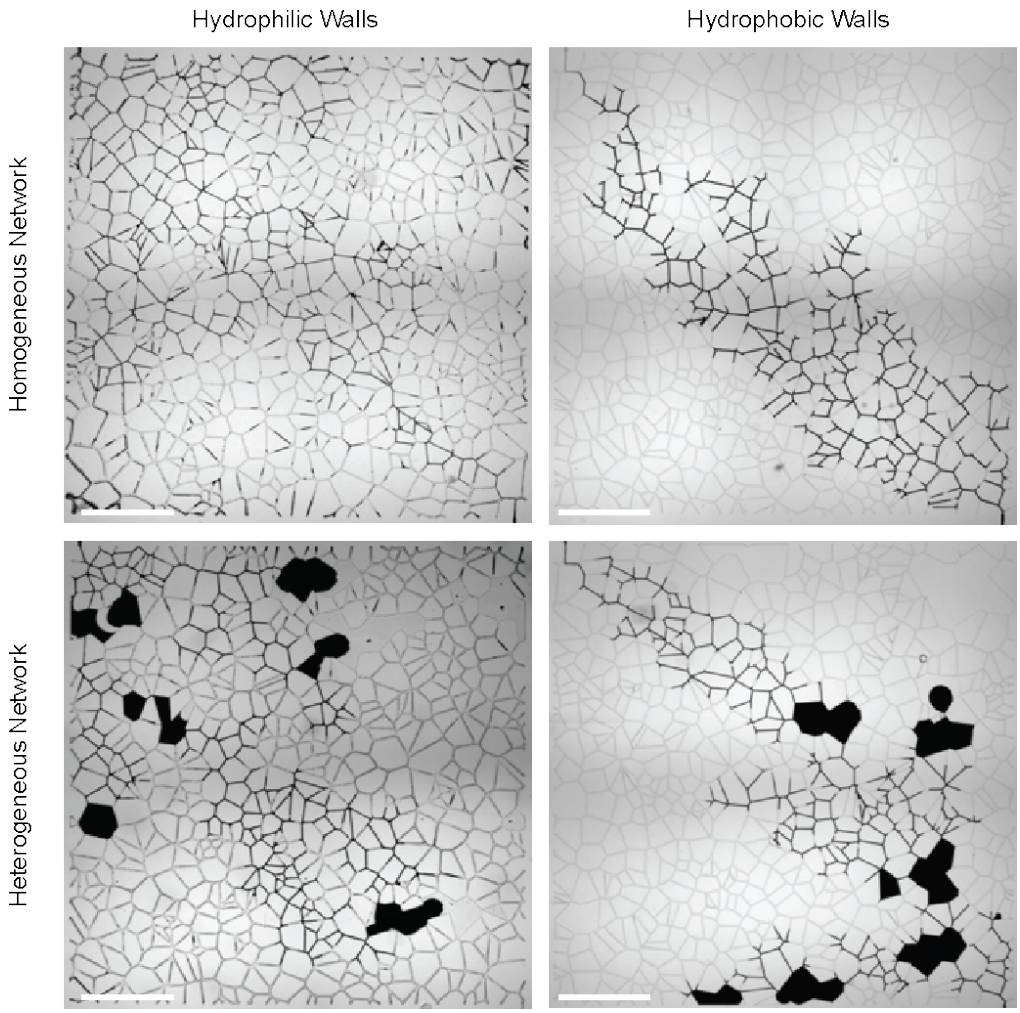

Figure 1-4: Displacement of oil (gray fluid) by water (black fluid) as a function of network topology and wetting.

The displacement pattern of the water was a function of both the network topology and wetting. The effect of wetting was the strongest determinant of the filling pattern. The filling pattern of hydrophobic walls resembles capillary fingering. In the case of hydrophilic walls, the water phase spontaneously fills the network, even in the absence of a pressure gradient. When a pressure gradient is applied, the filling pattern resembles a set of discontinuous capillary domains of water-rich and oil-rich areas. Network heterogeneities increase the branching of the pattern, especially in networks with hydrophobic walls. An observation of the transient filling of networks shows that water enters into a vug through one channel but exits through many. Figure 1-4 shows that the vugs in the hydrophobic case tend to divert the water from the more linear trajectory observed in the homogeneous case.

Our observation that water saturation in heterogeneous media is higher after breakthrough than that in homogeneous media seemingly conflicts with the conventional wisdom in reservoir engineering that heterogeneity reduces sweep efficiency. The disparate length scales between our micro-models and an actual

reservoir could explain this discrepancy. On the microscopic level considered in this study, there are good reasons to believe that isolated vugs increase the sweep efficiency. First, vugs act as excellent pressure conductors due to their low hydraulic resistance. Given their multiple contacts with the low-permeability channels, more area can be swept by the pressure gradient, leading to increased water saturation. Second, the porosity in the vugs is close to 100% swept from our image analysis, which will also increase the water saturation compared to that in homogeneous media. The question of at which scale the heterogeneity begins to reduce the sweep efficiency is an interesting one that warrants further study.

1.4 Conclusions and Future Work

Using the advanced nano-fabrication techniques originally developed in the semiconductor industry, we have developed novel pore scale models to investigate multiphase flows. These models contain pores that range from 100 nm to 10 μm, capturing the relevant length scales of many conventional and unconventional reservoirs. Future work in the upcoming year will focus on measuring the dynamics of gas-liquid flows at a 100 nm scale, understanding the relationship between coordination number and sweep efficiency, and building the next prototype of nano-fluidic devices.

2. Wettability tests to understand the interaction between hydraulic fluid compositions and rocks in macroscale

2.1 Introduction

Shale gas is the second largest unconventional energy resource after heavy oil. Shales have an abundance of organic matter (kerogen) that sets them among the best candidate source rocks for petroleum and natural gas generation. However, shale gas reservoirs present a unique problem to the petroleum industry. They contain natural gas in both the pore spaces of the organic matter as free gas and on the surface of the rock grains as adsorbed gas [1]. Two major enhancement techniques are used to extract natural gas from shale. Horizontal drilling is used to provide greater access to the gas trapped deep in the producing formation. Hydraulic fracturing unlocks the hydrocarbons trapped in shale formations by opening cracks (fractures) in the rock and allowing natural gas to flow from the shale matrix into the well.

Chemical additives such as friction reducers and viscosifiers often have been added to fracturing fluids. However, these additives may impair the fracture permeability and alter the rock wettability, which influences the gas flow ability. To remedy this problem, an intensive study of rock surface and fluid composition interaction should be performed in order to better understand the impact of induced fluid on rock surface wettability.

However, the mineralogy of the rock surface influences the overall wettability of the fluid-rock system. X-ray diffraction (XRD) technology is introduced to analyze the mineralogy of each sample so that an attempt can be made to build a relation between mineralogy and wettability. Then contact angle measurements are performed on the gas shale samples, and the effect of various fracturing fluid additives on their wettability are examined.

2.2 Experimental Methods

2.2.1 Materials

1) Gas shale

The gas shale tested here come from five sources, as listed in Table 2-1.

a. Haynesville Shale

The Haynesville Shale is situated in the North Louisiana Salt Basin in northern Louisiana and eastern Texas with depths ranging from 10,500 to 13,500 ft, as reported by Halliburton Energy Services. The Haynesville is an Upper Jurassic-age

Table 2-1: Examined gas shale sample data

Sample No.	Shale Play	Formation	Depth ft	Well Location	Field Name/Province
1	Haynesville[1]	n/a	12,000	Rusk County	Texas
2	Utica[1]	Indian Castle	4,649	St. Lawrence Lowlands between Montreal and Quebec City	Quebec, Canada
3		Dolgeville	4,878		
4		Dolgeville	5,197		
5	Fayetteville[2]	n/a	2,351	10N, range 16W, section 36	Van Buren, Arkansas

*(1. Baker Hughes Company; 2. Southwestern Energy Company)

shale bounded by sandstone (Cotton Valley Group) above and limestone (Smackover Formation) below [2], as shown in Figure 2-1.

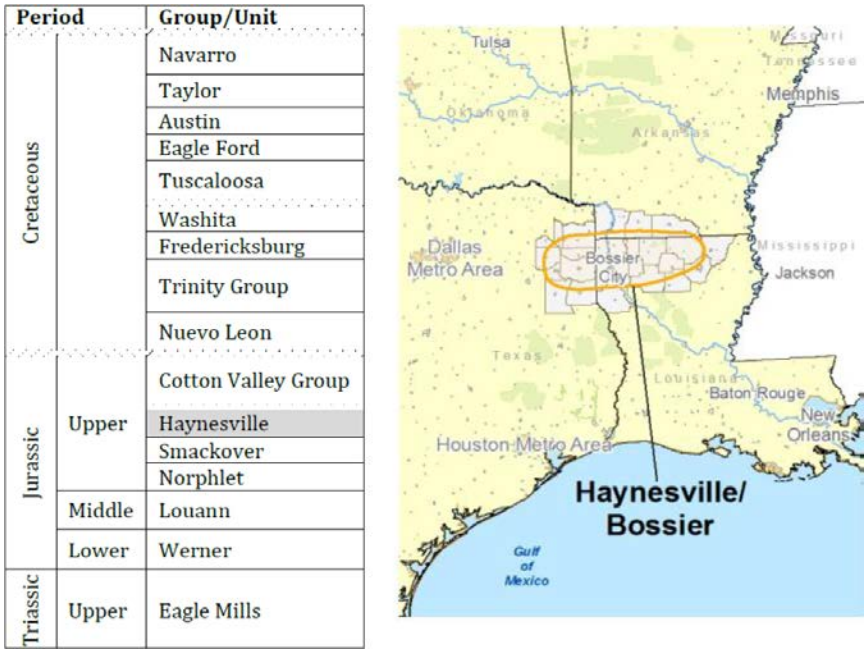

Figure 2-1: Stratigraphy and Location Map of the Haynesville Shale [3]

In 2007, after several years of drilling and testing, the Haynesville Shale made headlines as a potentially significant gas reserve, although its full potential will only be known after several more years of development. The daily gas production data reported by US Energy Information Administration (EIA) in the beginning of March 2011 show that the Haynesville Shale is currently producing about 5.5 Bcf, which surpasses the Barnett production by 0.25 Bcf, as presented in Figure 2-2. This

growth is attributed primarily to increasing drilling activities, improving the drilling experience and expanding the regional infrastructure of Haynesville Shale.

The Haynesville Shale covers an area of approximately 9,000 square miles with an average thickness of 200 to 300 ft, as estimated by Boughal [4] and Berman [5], respectively. The thickness and areal extent of the Haynesville has allowed operators to evaluate a wider variety of spacing intervals, ranging from 40 to 560 acres per well [6]). The Haynesville formation has the potential to become a significant shale gas resource for the U.S. with original gas-in-place estimates of 717 Tcf and technically recoverable resources estimated at 251 Tcf [7].

b. Utica Shale

The Utica Shale play lies between 3,000 and 7,000 thousand feet beneath the Marcellus Shale but extends further northwest and much further southwest of the Appalachian Basin region, as shown in Figure 2-2. Utica Shale consists of three members, Indian Castle at the top, Dolgeville in the middle and Flat Creek at the bottom. Utica Shale rocks are Ordovician in age, but Marcellus is Devonian shale.

According to the data provided by the EIA and the United States Geological Survey (USGS), the Utica Shale is thicker than the Marcellus and is much more geographically extensive (about twice as extensive as the Marcellus). Its thickness and widespread geographical extent indicate that it may become an enormous natural gas resource.

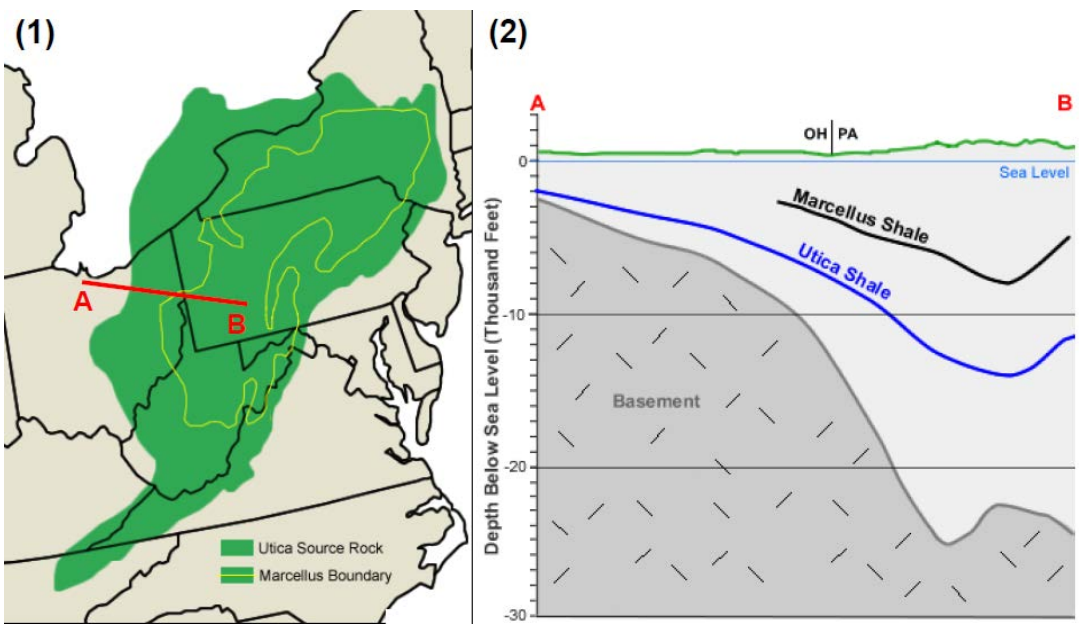

Figure 2-2: Utica Shale Gas Play Geographic and Cross-Section Map [8]

c. Fayetteville Shale

The Fayetteville Shale is situated in the Arkoma Basin of northern Arkansas and eastern Oklahoma over a depth ranging from 1,000 ft to 7,000 ft, as illustrated in

Figure 2-3. The Fayetteville Shale is a Mississippian-age shale bounded by limestone (Pitkin Limestone) above and sandstone (Batesville Sandstone) below [9].

Development of the Fayetteville began in the early 2000s. Between 2004 and 2007, the number of gas wells drilled annually in the Fayetteville shale jumped from 13 to more than 600, and its annual gas production increased from just over 100 MMcf to approximately 88.85 Bcf [4].

The area of the Fayetteville Shale play is nearly double that of the Barnett Shale at 9,000 square miles, with well spacing ranging from 80 to 160 acres per well and pay zone thickness averaging between 20 ft and 200 ft [10].

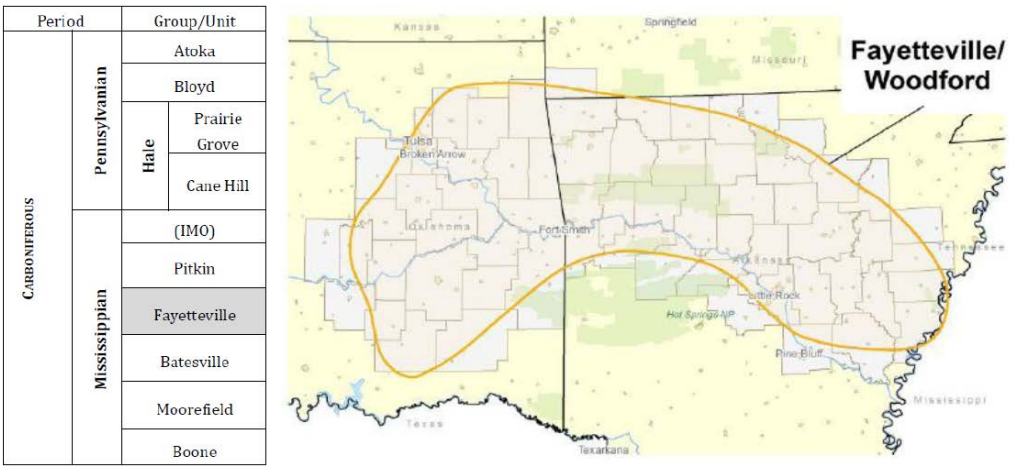

Figure 2-3: Stratigraphy and Location Map of the Fayetteville Shale [3]

2) Chemical additives during hydraulic fracturing

Six chemical additives are chosen to conduct the wettability study during gas shale hydraulic stimulation. They are the majority composition of fracturing fluids, all from BJ Service (now the Baker Hughes company, TX). The six additives are comprised of two polymers (FRW-18 and FRW-20) and four surfactants (Inflo-45LB, Inflo-250, GasFlo-G, and Flowback-30). FRW-18 and FRW-20 are friction reducers, which could reduce the friction between the pipe and hydraulic fracturing fluids, therefore helping to make the water easier to pump and reducing the amount of equipment needed. FRW-18 has been used as a friction-reducing agent in slickwater fracturing for some time, while FRW-20 is a new product featuring easilybreakable chemistry, which causes little or no formation damage [11]. Inflo-250 is a non-ionic surfactant product which would enhances the mobilization of liquid and reduces the flowback period and overall job cost without adversely affecting production. Its cost is significantly less than commodity additives with comparable downhole performance. GasFlo-G is a surface tension reducer that can stabilize the mixture of oil and water by reducing the surface tension where the two molecules meet to aid in the distribution and recovery of fracturing fluids. All of these examined solutions were made of 0.1% wt. concentration and prepared using distilled water. Each solution is stirred at 700 RPM for 2-72 hrs on the stir plate (Fisher Science, MA).

2.2.2 Equipment

1) X-Ray Diffraction and Clay Mineralogy

Compositionally, clay minerals fall into the class of aluminum silicates; structurally, they are complex with a wide range of properties. The basic building blocks are silica tetrahedral and aluminum octahedral. Carbonate minerals are commonly associated with clay minerals, especially calcite and dolomite.

These very fine-grained minerals can be better analyzed by X-ray methods than by hand specimen or optical methods. An XRD (XDS 2000; Scintag Inc., Sunnyvale, CA) is employed, which uses nickel-filtered Cu K_α radiation (λ=1.5405 Å) in a step-scan mode with 2θ =0.01° per step.

Moreover, clay structures are three-dimensional and vary considerably from one type of clay to another. X-Ray diffraction is considered the best method in defining clay minerals. The qualitative identification procedure begins with searching for a mineral that has the strongest peaks, followed by confirming the choice by finding the positions of weaker peaks for the same mineral. The most important relationship in X-ray diffraction [12] is:

$$n\lambda = 2d \sin\theta \qquad (2\text{-}1)$$

where n is an integer (i.e., 1, 2, 3…, etc.), λ is the wavelength of the incident X-ray beam (1.54 Å for Cu), d is the distance between atomic layers in a crystal, and θ is the angle between the incident ray and the scattering planes. The diffraction planes are 00l= (001), (002), (003), (004).

Creating a sample preparation for XRD analysis of clay minerals is probably the most critical step. The problem is how to free individual crystallites of clay from the rock or sediment without damaging them in any way, physically or chemically, and then to prepare ordinated amounts that will satisfy the requirements for X-ray analysis. Much has been written on this aspect of analysis, and different authors favor different procedures. Some of these procedures are time-consuming and quite involved; some require equipment that is not readily available.

A good discussion of a sample preparation and its problems appears in Moore and Reynolds [13]. Here, we adopt a procedure described originally by Austin and Coose [14] and modified by Dr. David Wronkiewicz, Missouri University of Science and Technology. The procedure described below is for identification only; it allows most common clays to be identified but ignores many of the potential problems in favor of simplicity and speed:

a) The sample is crushed to a fine powder. Unfortunately, this will reduce all minerals to clay size so that they cannot be separated from the clay minerals;
b) The sample is disaggregated in distilled water. There are several ways to accomplish this. The simplest way is to put 5-25 grams of the sample in a

covered vial with distilled water and shake vigorously. If there is flocculation during the next step, then a peptizing agent such as Clagon or NH_4OH is used before agitating;

c) A clay fraction is separated from the coarser material. If the disaggregated sample is allowed to stand for 10 minutes, the coarse fraction will have settled, and the clay and some silt will remain in suspension; longer setting times are required for better separation. The amount of suspended clay depends on the relative volumes of the sample and distilled water, and on the amount of clay in the sample;

d) The clay sample is then mounted on a glass slide. To accomplish this step, the pipette or eye dropper used to draw off some of the clay-water slurry prepared in Step 3 was exploited. The entire glass slide was covered completely with the slurry but without causing it to overflow. Then, the slide was allowed to dry overnight at room temperature.

e) Finally, the glass slide was brought into θ: θ goniometer for XRD analysis.

The specimens were examined three times on an XRD instrument under different circumstances. Sometimes it is difficult to distinguish between chlorite and kaolinite when only weak peaks are present at 12.5° and 25° 2θ. Such a sample could contain only chlorite, only kaolinite, or a mixture of the two. In this situation, the sample is treated chemically or heated and then reexamined. To eliminate any interference between the peaks of different clay minerals, the following procedure was implemented. Initially, the samples were examined before applying any treatment, and the resulting run was marked as "Untreated." Then, the samples were put in a glycolation vessel for 24 hours to widen the clay mineral layers for better mineral identification resolution. This run was called the "Glycolated" run. The last run was performed after heating the samples up to 375°C for 1 hour, and it was named the "Heated" run.

2) Contact Angle

When only one fluid exists in the pore space, only one set of forces, the attraction between the rock and the fluid, must be considered. When more than one fluid phase is present, at least three sets of active forces, solid-liquid interfacial tension (γsl), solid surface tension (γsv) and liquid surface tension (γlv), will affect capillary pressure and wettability, as presented in Figure 2-4..

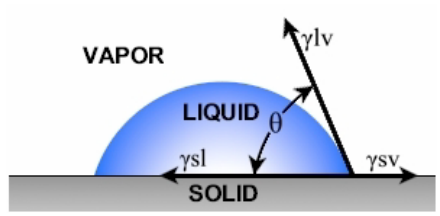

Figure 2-4: Equilibrium of Forces at Liquid-Vapor-Solid Interface

Rock wettability basically is defined by the contact angle measurement. The goniometer presented in Figure 2-5 (Model 500 Advanced Goniometer, Rame Hart,

Succasunna, NJ) is exploited to measure the contact angle of various fluids on the shale rock surfaces.

Figure 2-5: Contact Angle Goniometer Instrument

The resulting contact angle measured by the goniometer device, which uses a sessile drop technique, is defined by the following equation:

$$\theta = 2\tan^{-1}\frac{2h}{d} \tag{2-2}$$

where θ is the contact angle, h is the drop height and d is the drop diameter or width.

Polished plates of shale gas samples were used as representative surfaces for sessile drop and contact angle measurements. In our measurements, the specimen does not account for surface roughness, material heterogeneity or the presence of organic matter. Alternative wettability measurement methods suggested by Tiab and Donaldson [15] could be one of the best tools for studying shale gas wettability. All of the presented results were repeated at least three times for each shale chip.

2.3 Results and Discussions

2.3.1 X-Ray Diffraction and Clay Mineralogy

By using basal spacing (d) and 2-theta for Cu K_α radiation in Table 2-2, clay and non-clay mineral peaks can be distinguished readily. Some mineral peaks may be invariant because the mineral structure does not tolerate significant atomic substitutions. We focus on small diffraction angles because most of the important clay peaks occur at 2-theta values of 40° or less; therefore, theta is 20° or less, and that value is sufficiently small to fit the foregoing argument to a reasonable approximation.

Yaalon [16] applied normative calculations on the chemical composition of 10,000 shales and arrived at the following average composition: 60% clay minerals (mostly

Table 2-2: Basal Spacing (d) in Å and 2θ for Cu K-Alpha Radiation*

Clay Mineral Group	001		002		003		004	
	Å	2θ	Å	2θ	Å	2θ	Å	2θ
Chlorite	14.1-14.2	6.2-6.3	7.05-7.1	12.5-12.6	4.7	18.9	3.52-3.54	25.3-25.1
Kaolinite	7.16	12.4	3.57	24.9	2.38	37.8	1.78	51.3
Mica (Illite)	9.97-9.98	8.8	4.96	17.9	3.32	26.8	2.49	36.1
Ca Smectite** Na Smectite	15.4-12.4	5.7 7.1	7.7 6.2	11.5 14.3	5.1 4.1	17.4 21.7	3.8 3.1	23.4 28.8
Ca Smectite - glycol Na Smectite - glycol	17-16.7	5.2	8.5	10.4	5.7	15.6	4.2	21.2
Vermiculite	14.1-14.3	6.3		w		w		w
Non-Clay Minerals								
Calcite		29.5						
Dolomite		30.9						
Quartz		20.8		26.6				
Albite and Microcline		27.7						
Pyrophyllite		9.6		19.3		29.1		

** General position of broad peaks
w = weak if present at all

illite), 20% quartz, 10% feldspar, 6% carbonates, 3% iron oxide, and 1% organic matter. This agrees with the presented XRD results.

Table 2-3 presents a summary of the semi-quantitative analysis of XRD results. Semi-quantitative assessments make the identification of individual minerals in shale gas samples much more valuable. Unfortunately, the intensity of a mineral's diffraction peaks cannot be used directly as an accurate measure of mineral abundance because different minerals, different atomic planes within a mineral, and different samples of the same mineral do not have the same ability to diffract X-rays [17]. However, this study used the modified procedure for the semi-quantification of clay minerals with an approximate accuracy of ±10%. The computed clay mineral contents often were avoided because of their weak or doubtful peak intensity.

Figure 2-6 presents a combined plot of XRD results for five shale gas samples. Utica shale sample obtained from Indian Castle formation and Haynesville shale exhibit the highest amount of illite, where the first strongest peak at 8.8° 2θ is obvious. Both of the Utica shale samples acquired from the Dolgeville formation are classified as calcareous shale. XRD results also suggest high calcite content. Fayetteville shale may compositionally consist of higher quartz content than illite because illite's peak intensity is almost nonexistent.

Table 2-3: Summary of Qualitative XRD Results

Shale Gas Source Rock Samples		Haynesville Shale 12,000 ft	Utica Shale Indian Castle Fm. 4,649 ft	Utica Shale Dolgeville Fm. 4,878 ft	Utica Shale Dolgeville Fm. 5,197 ft	Fayetteville Shale 2,351 ft
Clay minerals	Chlorite	31%	Low	-	-	-
	Illite	69%	High	V. Low	V. Low	Low
Non-Clay minerals	Calcite	Low	Low	High	High	V. Low
	Dolomite	-	V. Low	-	V. Low	V. Low
	Quartz	Moderate	Moderate	V. Low	V. Low	High
	Albite and Microcline	-	Low	-	-	-

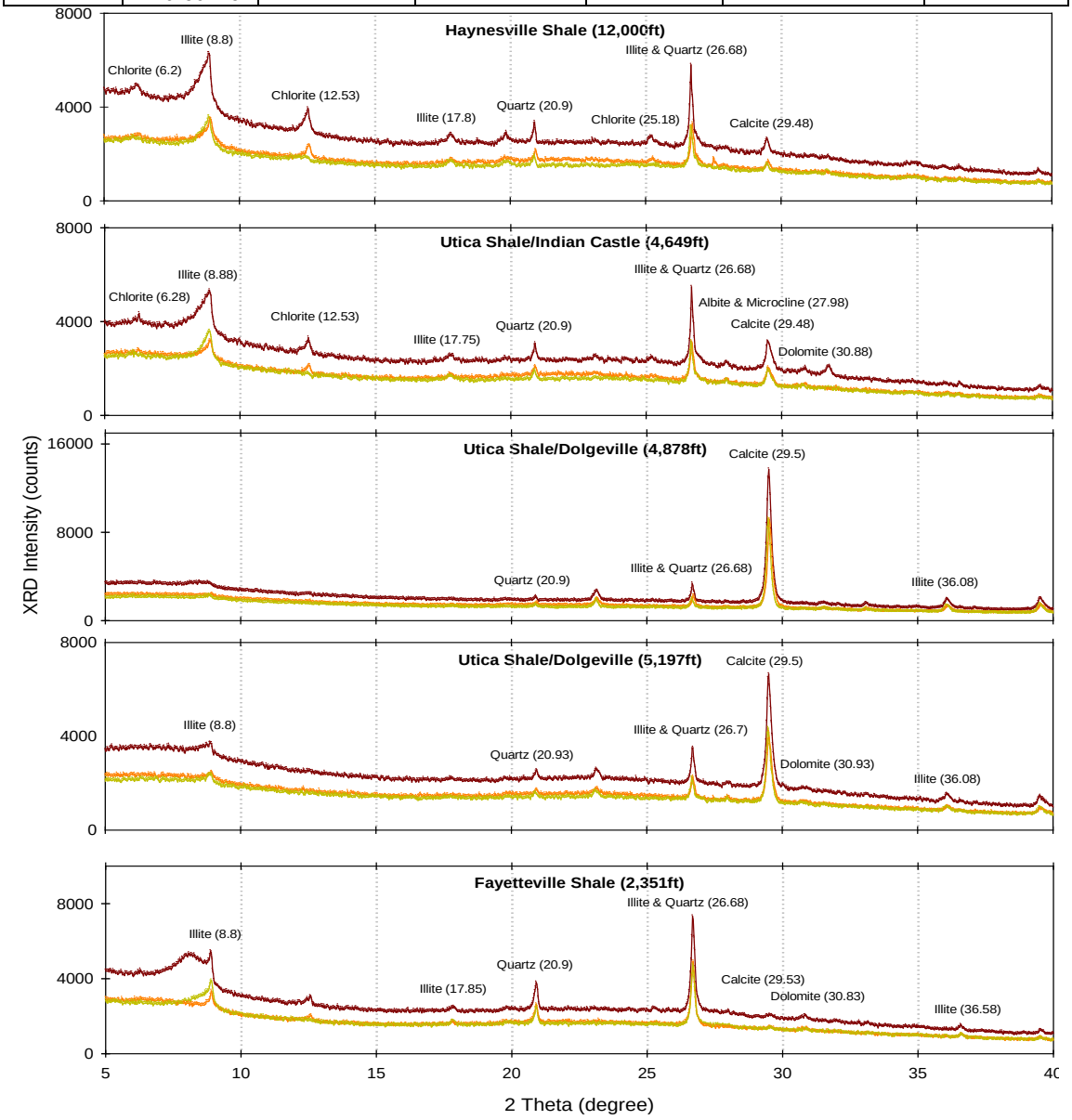

Figure 2-6: X-ray diffraction results of the five shale gas samples.

2.3.2 Contact angle

The obtained contact angle measurements from five shale samples using six chemical additives of fracturing fluid are presented in Figure 2-7.

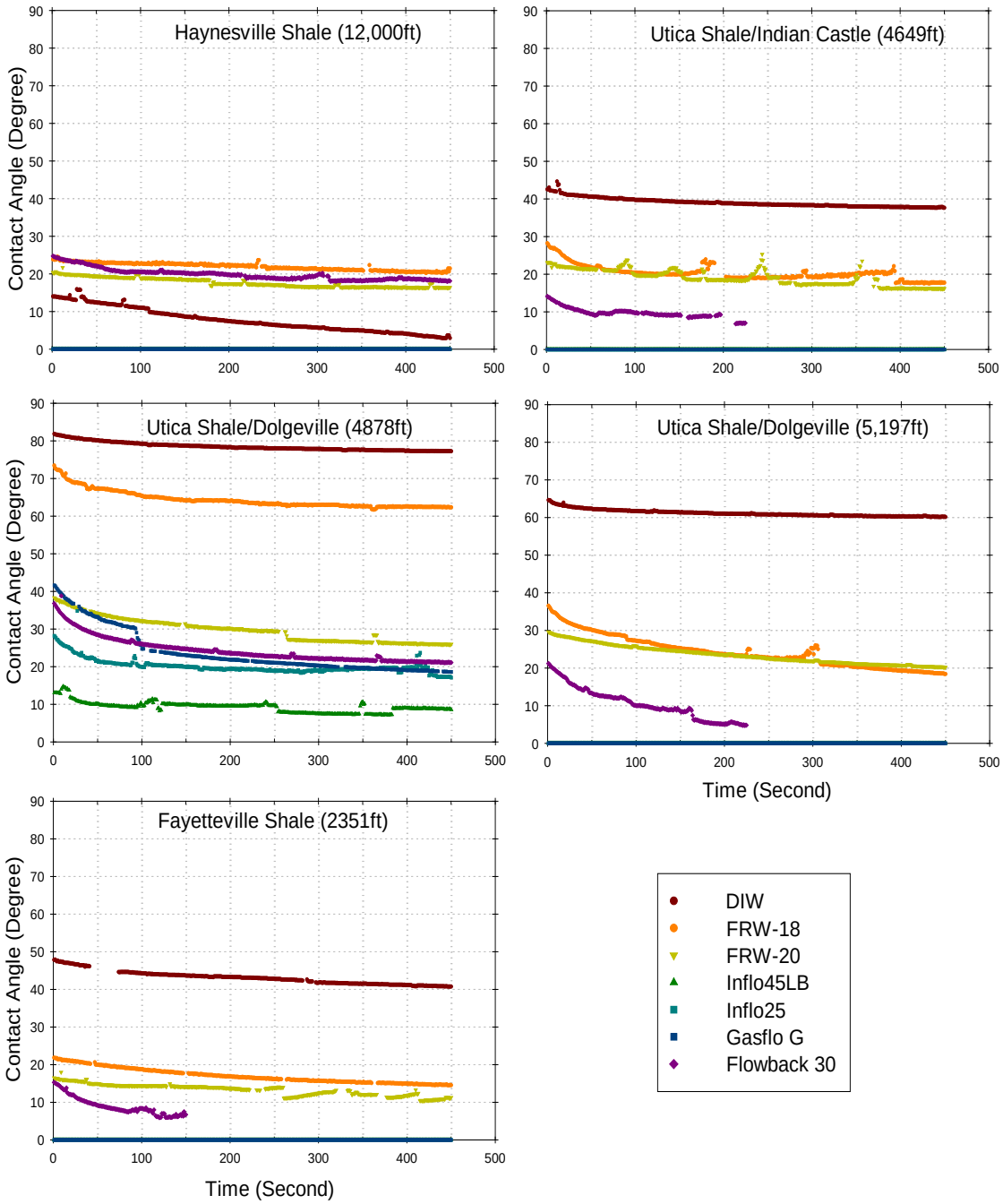

Figure 2-7: Contact angle results of the five shale gas samples using six fracturing fluid additives.

All contact angle results were compared to the contact angle of deionized water (DIW) and are summarized in Table 2-4.

Clearly, all the fracturing fluid additives tested on Utica and Fayetteville shale rock samples resulted in a reduced contact angle and shale rocks that behave more like water-wet surfaces compared to DIW contact angles. The scenario for the Haynesville shale sample is slightly different; both polymers and the Flowback-30 surfactant tended to increase the contact angle slightly to an intermediate water-wet level. This might be attributed to (1) a very high illite concentration (70%), as illite's peak intensity on XRD data suggests, and (2) a low organic matter content of Haynesville shale (TOC = 0.81 wt. %).

Table 2-4: Contact Angle Results Summary*

Gas Shale Source Rock Samples	Haynesville Shale 12,000 ft	Utica Shale Indian Castle Fm. 4,649 ft	Utica Shale Dolgeville Fm. 4,878 ft	Utica Shale Dolgeville Fm. 5,197 ft	Fayetteville Shale 2,351 ft
DIW	14.0	42.5	81.8	64.6	47.8
0.1% FRW-18	23.8	28.2	73.4	36.5	21.8
0.1% FRW-20	20.4	23.1	38.3	29.6	16.5
0.1% Inflo-45LB	0.0	0.0	13.0	0.0	0.0
0.1% Inflo-250	0.0	0.0	28.2	0.0	0.0
0.1% GasFlo-G	0.0	0.0	41.6	0.0	0.0
0.1% Flowback-30	24.7	14.1	36.8	21.2	15.3

* Contact angle results have an accuracy of ± 5 deg.

Clearly, all the fracturing fluid additives tested on Utica and Fayetteville shale rock samples resulted in a reduced contact angle and shale rocks that behave more like water-wet surfaces compared to DIW contact angles. The scenario for the Haynesville shale sample is slightly different; both polymers and the Flowback-30 surfactant tended to increase the contact angle slightly to an intermediate water-wet level. This might be attributed to (1) a very high illite concentration (70%), as illite's peak intensity on XRD data suggests, and (2) a low organic matter content of Haynesville shale (TOC = 0.81 wt. %).

Utica shale samples acquired from the Dolgeville formation result in the highest DIW contact angle, which is between 60 to 80°. This rock behaves like oil-wet material. X-ray diffraction results suggest a high concentration of calcium carbonate (calcite). However, the Utica shale sample acquired from the Dolgeville formation at a depth of 4,878 ft behaves slightly differently when treated with all surfactants and polymer FRW-20. These solutions have the tendency to alter the wettability of this rock to water-wet with contact angles of 10° to 30°. Polymer FRW-18 very slightly shifts this surface's wettability toward water-wet, which is attributed to the fracturing fluid's chemical composition and clay mineralogy. This sample is classified as calcareous shale, sometimes also called carbonate-like shale. This rock sample is very hard to saw, which likely can be attributed to (1) a very high lime content, as calcite's peak intensity in XRD results suggests, and (2) an extremely low organic matter content (TOC = 0.31 wt. %), as documented by Elgmati and Zobaa

[18]. According to Leverson [19], Perrodon [20] and Wang and Reed [1], organic substances are oil wet.

In the most commonly-presented cases, surfactant solutions alter shale wettability to strongly water-wet conditions, except for surfactant Flowback-30, which behaves like the polymers. Both polymer solutions alter the wettability of shale gas rocks in the same manner, with resulting contact angles of 20° to 30°, except for the Utica shale sample acquired from the Dolgeville formation at a depth of 4,879 ft. For this shale sample, only polymer FRW-18 results in a high contact angle of 62°.

In summary, shale gas wettability changes to oil-wet when a high concentration of calcite exists. Organic matter content governs the fracturing fluid's wettability alteration. Low organic matter content tends to change the wettability of calcareous samples to oil-wet .

Calcite content proved the dominant factor in increasing the shale gas contact angle and changing the wettability of shale gas rock to oil-wet. Organic matter content governed the wettability alterations of calcareous samples.

2.4. Conclusions

XRD mineralogy analyses and contact angle measurements were conducted, yielding the following observations and recommendations:

a) XRD analysis provided insight into clay and non-clay mineralogy. It showed high illite content in the Haynesville and Utica shale samples and also suggested high calcium carbonate (lime) content in the Utica shale samples;
b) Calcite content proved the dominant factor in increasing the shale gas contact angle and changing the wettability of shale gas rock to oil-wet. Organic matter content governed the wettability alterations of calcareous samples;
c) The effect of induced fluids, such as hydraulic fracturing additives, on wettability alteration and the impact of that alteration on permeability and porosity require further study. This could be accomplished with imbibition and membrane setup.

2.5 Future work

Wettability alteration evaluation

During hydraulic fracturing of the shale gas reservoir, million gallons of water-based fracturing fluid is pumped into the reservoir, generating fractures or micro-fractures. After treatment, the significant amount of water remaining in the fractures or having penetrated into the matrix can easily create a water block, thus decreasing gas productivity or damaging the formation.

Kewen and Abbas [21] posited a definition of gas-wetting in which neither water nor oil spontaneously imbibes in cores with chemically-altered wettability states.

They proposed to enhance gas well production by altering the wettability to preferential gas-wetting.

A procedure is developed to evaluate the wettability alteration, as shown in Figure 2-8.

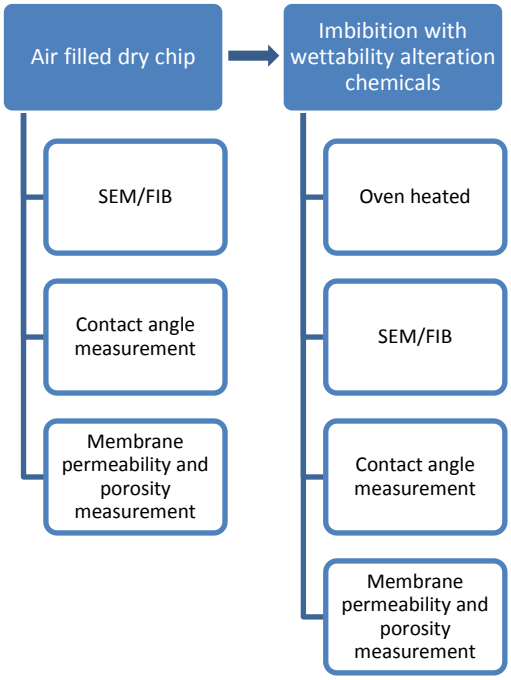

Figure 2-8: Flowchart of wettability alteration evaluation

Before the imbibition test, the pore structure of the dry core will be characterized first by the FEI Helios NanoLab 600 FIB/SEM, which is intended for simultaneous site-specific FIB cross-sectioning and high-resolution nondestructive SEM imaging, available at Missouri S&T. Then, a goniometer will be used to check the wettability of shale core with water. Finally, a membrane setup will be implemented to measure permeability and porosity.

After the imbibition test, the treated shale core will be dried in the oven. The following tests will be performed, and the results will be compared with the values before imbibition. SEM imaging yields the chemical adsorption on the rock's surface. The contact angle results indicate the gas-wet condition, and membrane tests show any damage or improvement to the formation.

2.5.1 Imbibition method

In order to select chemicals that show good wettability alteration without causing significant damage to the permeability of the cores, imbibition tests will be conducted first, as shown in Figure 2-9. Given the extremely low permeability, an air-filled shale or tight gas sandstone is secured on a line, immersed in chemical solution and connected to a digital stress detector. However, when using this imbibition, a long time may be required to ensure that the core is fully saturated.

Therefore, the chemical solution is covered with an oil film on top and a cap above to prevent the solution from evaporating. The weight shown by the digital detector is recorded with the time in the data acquisition system.

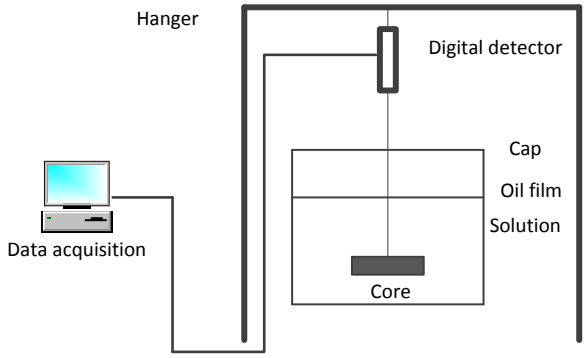

Figure 2-9: Schematic of imbibition setup

After days of imbibition, once the weight changes of the core slow down, one test is considered finished. The relationship between the imbibition rate and time would be easy to generate.

2.5.2 Membrane permeability measurement

Considering the physical properties of the membrane, such as its extremely low permeability, a conventional core-flooding experiment would not be feasible for the permeability measurement. A membrane setup is designed to solve this problem, as shown in Figure 2-10.

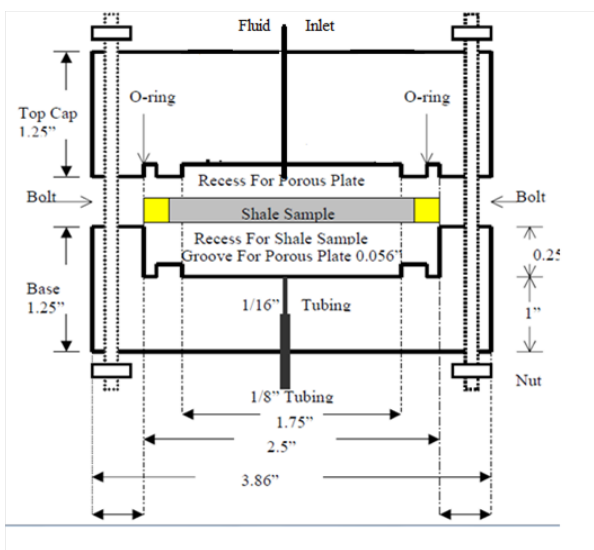

Figure 2-10: Schematic of membrane setup

Membrane technology usually is used in drilling fluid filtration tests and has been applied to well logging. Only recently has this technology been employed for core analysis, and it shows propitious results [22].

3. Nano-fluidic chip experiments to understand fluid flow on nano-scale pore spaces and cracks

Part I. Liquid flow behavior in micro-scale channels that mimic micro-fractures in shale gas formation

3.1 Introduction

Over the past few decades, the advent of single-molecule imaging has revolutionized the measurement of physical parameters, chemical/biochemical reactions and interactions because the data is obtained in real time, not by averaging. Combined with micro-fluidic and nano-chips, this technique has been used widely in biological and toxicological research to study molecule-molecule interactions, molecule-cell interactions, nano-particle-cell interactions, cell functions, etc. However, single-molecule imaging has not been used to study the flow behavior of natural gas and introduced fluids (water, surfactant solutions and polymers) in nano-Darcy range of tight gas and shale formations.

Meanwhile, advances in micro-system fabrication technologies have provided increasing numbers of structures miniaturized on the micro-meter and nano-meter scales; in other words, the dimensions of these structures are comparable to the size of tight shale pores and macromolecules. Thus, a better understanding of the introduced fluid flow behavior in tight gas and shale formations will be achieved using a single-molecule imaging detection technique combined with nano-fluidic chips.

3.2 Experimental methods

3.2.1 Materials

A Commercial Friction-Reducing Polymer: FRW-20 was provided by BJ Services in Tomball, Texas. Basic properties of the polymer are shown in Table 3-1. Fluorescein (Table 3-2) was used as fluorescent dye for the aqueous solution. FRW-20 was diluted to 0.1% by lab reagent water; then, the mixture was vortexed for 1 min and subjected to ultra-sonication for 5 min. Fluorescein was prepared in lab reagent water to 10^{-5} Mole/L to generate a fluorescent signal. Then, a 5% fluorescein stock solution was added to the polymer solution.

Chemicals for linear PAM capillary coating, include acrylamide, ammonia persulfate, fluorescein, MAPS and Tetramethylethylenediamine (TEMED) were purchased from Sigma Aldrich (St. Louis, MO, USA)

Capillary tubes were served as micro-scale channels. All capillary tubes were purchased from Polymicro, Inc.

Table 3-1: Basic information of FRW-20

Name	CAS#	Percent	Solubility in water	pH	Viscosity (F)
FRW-20	064742-47-8	10-30	Dispersible	8.5	576.0cps @75 ˚F

Table 3-2: Basic information of fluorescein for polymer labeling

Compound Name	CAS#	Molecular formula	Solubility in water	excitation wavelength	Emission Wavelength
Fluorescein	2321-07-5	$C_{20}H_{12}O_5$	slightly	494 nm	521 nm

3.2.2 Micro-/Nano-model preparation

Square capillary tubes were used to study the polymer/decane flow profile. Circular capillary tubes were used to study the flow and aggregation behavior of polymer particles. All sample channels were rinsed with pure water and methanol first and then dried by blowing air for 15 min. The bare capillary tubes were served as hydrophilic inner surface micro-channels. Linear PAM-coated capillary tubes served as hydrophobic surface micro-channels. Capillary tubes were coated using the procedure described below:

The capillaries first were rinsed by 1M HCl, 1M NaOH and methanol for 5mins; then, they were filled with a methanol/MAPS mixture (1:1) and incubated at room temperature for 15 hours. After incubation, the capillaries were rinsed with methanol and water for 10 mins for each liquid; the capillary then was filled with an acrylamide reaction reagent that remained in the capillary for 2.5 hours. After the treatment, the capillary was rinsed with water and blow-dried with nitrogen gas for 10mins.

3.2.3 Experimental setup

Single Molecule Detection System**:** Single-molecule systems were optimized for the purpose of this study. The Ar+ laser (40 × NA, 0.75 objective) was used as the excitation beam, and the excitation wavelength was set to 488nm for most of experiments. Unless specified, the laser power was set at 5 mW before reaching the sample channels.

All images were captured by a reverse microscope (Olympus, IX-51) and high-speed ICCD camera. The ICCD camera was operated at -20 °C; for the work in the micro-scale model, the gain and exposure times were set at 80 and 50 ms, respectively. The delay of the shutter driver was set to 10 ms. Data were acquired through the Cellsens software provided by Olympus. The optic system is shown in Figure 3-1, which was optimized as well after the installation of the reverse microscope. The scheme of the the localized probing region of the micro-model on the single-molecule imaging system appears in Figure 3-2.

Fluid Transfer System**:** Figure 3-3 shows the experimental setup for the micro-scale channels. The capillary tube (Polymicro, Phoenix, AZ) was used as the sample channel for all experiments, with a 1 cm window cleared in the middle. TFE tubing was connected to one end of the capillary, and the other end of the tubing was

connected to two syringe pumps to facilitate linking to the polymer solution and decane reservoirs, respectively, which were held to a micro-state with a constant height to apply the desired hydrodynamic flow. A pressure transducer was used at the front of the capillary tube to measure the inlet pressure.

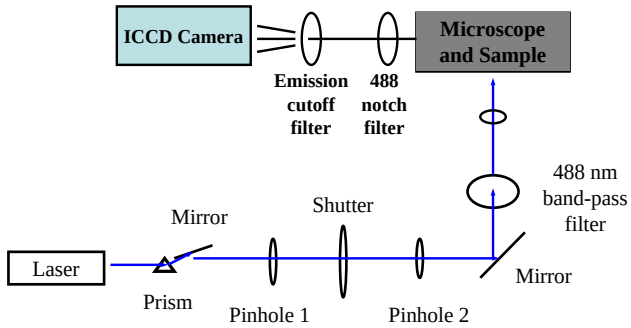

Figure 3-1: Optical arrangement for single-molecule detection system

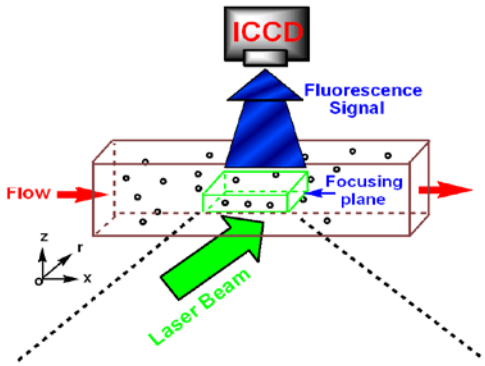

Figure 3-2: Localized probing region of single-molecule imaging system

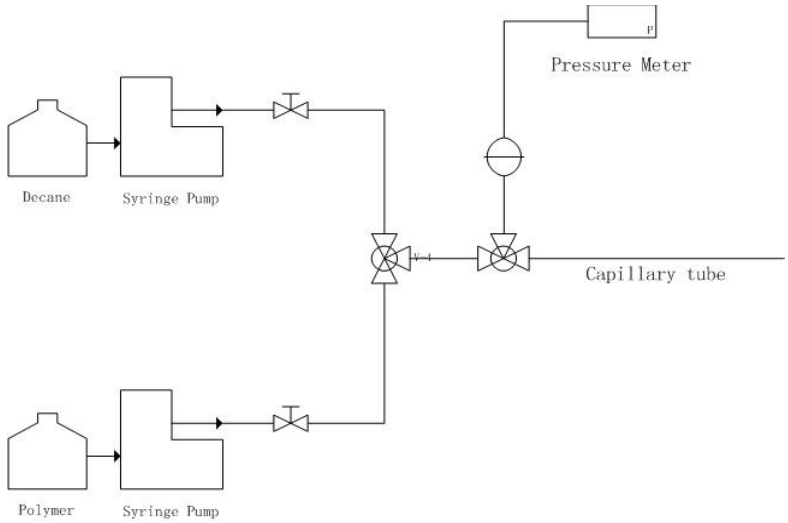

Figure 3-3: Experimental setup: Fluid transfer system

3.2.4 Characterization of the wettability conditions and sizes of modified micro-channels

The wettability of modified silica micro-channels can be determined by characterizing the aqueous static contact angle (h) of their inner surfaces. Those inner surfaces can be determined by measuring water-meniscus heights within the micro-channels.

3.2.5 Experimental procedure

1) Polymer/decane flow profiles: Effect of channel size and length on the initial pressure of the micro-channel

In order to understand the interaction and flow profile of polymer/decane, square capillary tubes were used as sample channels. The capillary tube was prefilled with decane. Fluorescein-labeled polymer solution was introduced into the capillary tube using the syringe pump. The injection pressures of the polymer solution into the micro-channels were measured by the pressure transducer. Experiments were conducted with different micro-channel dimensions (length and inner diameter) in order to study the effect of channel sizes (I.D) and channel lengths on the initial pressure of the micro-channel.

2) Polymer/decane flow profiles: Effect of channel size and length on the mobility of the interface

Interfaces between the polymer solution and decane were investigated within the micro-scale models. The operation procedure was the same as in 5.1. The interface between the polymer solution and decane was captured by the microscope equipped with the ICCD camera. The mobility of interfaces was calculated, and the shapes of the interfaces were characterized. Experiments were conducted under different lengths and sizes of sample channels.

3) Effect of channel size and wettability on the flow behavior of polymer particles

To investigate the flow behavior and aggregation configuration of polymer particles (micro-spheres), the polymer solution was first pretreated by diluting it with reagent water to a desirable concentration (0.1% v/v), and then it was ultrasonicated and vortexed prior to use. Then, the polymer solution (0.1% FRW-20) labeled 10^{-6} Mole/L fluorescein was introduced into the capillary by a KDS-100 syringe pump.

Table 3-3: Experimental conditions

Capillary ID (μm)	Lengths (cm)	Flow rate (ml/hr)
25	7.5	0.01
50	10	0.02
100	12.5	0.05
225	15	0.2

Experiments were conducted under different capillary lengths and sizes and different flow rates. The initial pressures of the capillary tubes were measured by a digital pressure gauge, and the velocities of the polymer micro-spheres were calculated. Two-hundred independent measurements of the micro-sphere velocities in micro-channels were taken to verify the repeatability, and the reported data represent the average.

3.3 Result and discussion

3.3.1 Experimental setup optimization

See Experiments section.

3.3.2 Polymer/decane fluid flow behavior in micro-models

Effect of channel dimensions and wettability on the capillary pressure of micro-channels: Polymer and decane

We used the in-house build single-molecule imaging system to measure and characterize the effect of channel dimensions, wettability and introduced fluids on the initial pressure of the micro-scale channel with the presence of two fluids, polymer/decane. Results are shown in Figures 3-4 through 3-7.

Figures 3-4 and 3-5 indicate that among channels with the same diameter, longer channels always have a higher capillary pressure than shorter ones; when the lengths are equal, channels with larger diameters always have a lower capillary pressure than those with smaller diameters. As shown in Figure 3-6, injection with polymer/decane yields a lower capillary pressure than injection with water/decane, which provides evidence that different introduced fluids affect the capillary pressure. The friction reducer (polymer solution) does reduce the pressure (or the resistance) of the channels.

Surface wettability also plays an important role in the capillary pressure of polymer/decane fluids. As seen in Figure 3-7, given channels with the same dimensions, hydrophobic channels have less capillary pressure than hydrophilic channel. With all other conditions being equal, the initial pressure was higher with longer capillary tubes; with capillary tubes of the same length, the pressure was higher with smaller diameters of capillary tubes.

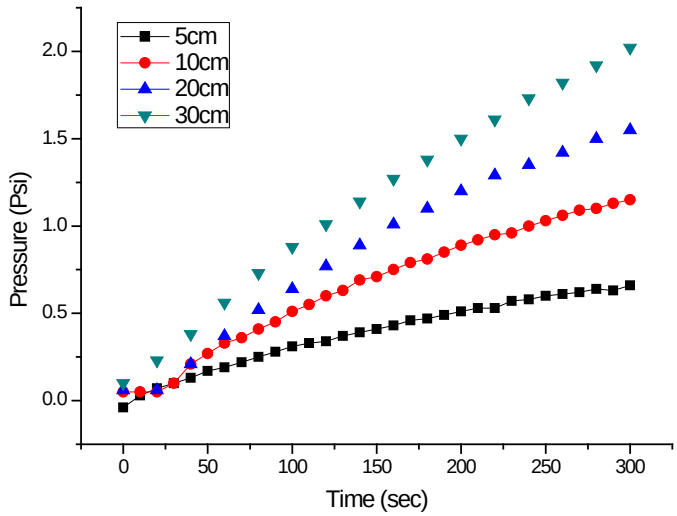

Figure 3-4: Initial pressure vs. time with different capillary lengths (capillary ID = 100μm, flow rate = 1.0ml/h)

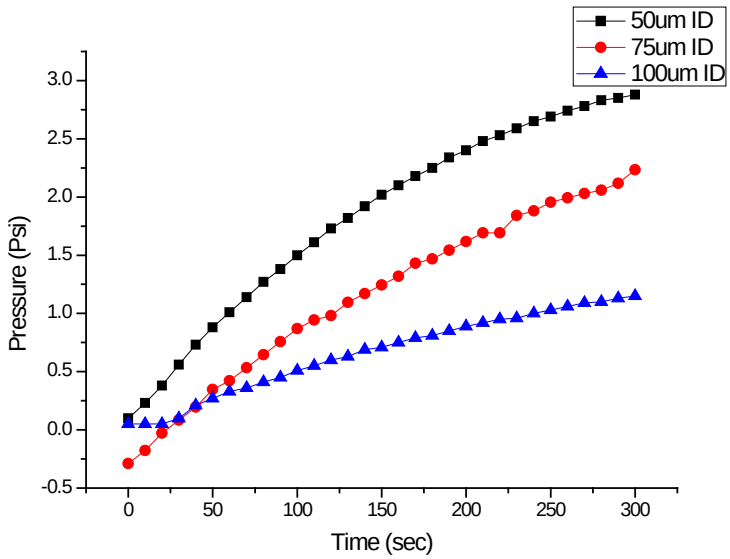

Figure 3-5: Initial pressure vs. time with different capillary sizes (capillary ID = 100μm, flow rate = 1.0ml/h)

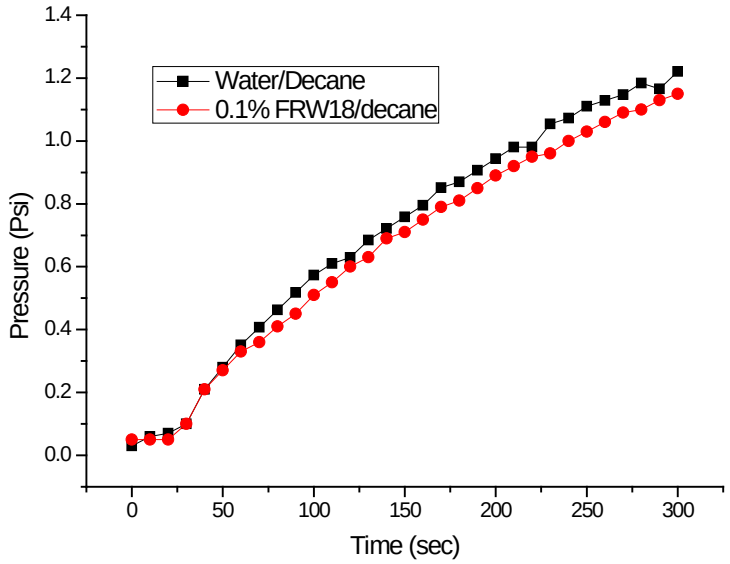

Figure 3-6: Initial pressure vs. time with water compared to polymer solution (friction reducer) (capillary ID = 100μm, flow rate = 1.0ml/h)

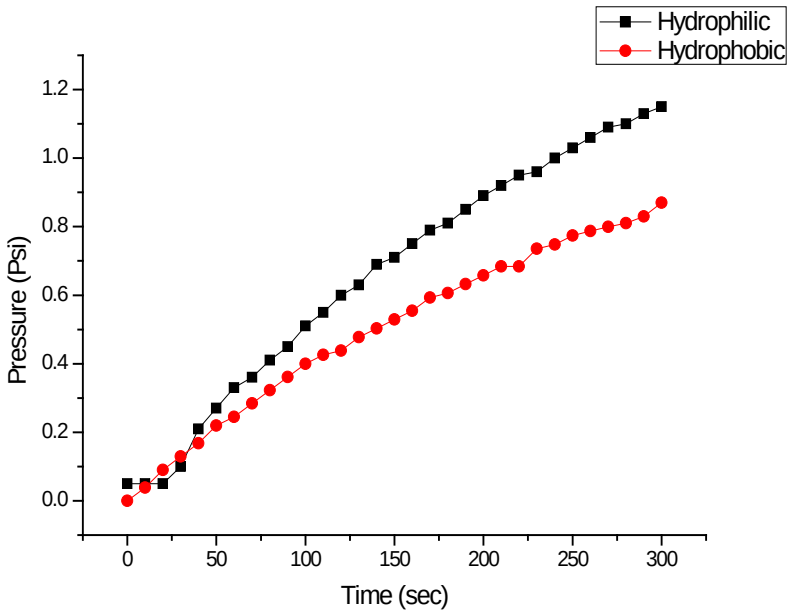

Figure 3-7: Initial pressure vs. time with different wettability channels (capillary ID = 100μm, flow rate = 1.0ml/h)

Flow behavior of two liquids, polymer and decane, in micro-scale channels: Mobility and shape interfaces

Clear interfaces between the polymer solution (FRW-18) and decane were observed, which means that they do not dissolve into each other. The particle imaging velocimetry (PIV) method was applied to capture the image of the interfaces, and the data were processed. Figures 3-8 through 3-11 show the mobility of interfaces between the polymer solution and decane in different dimensions of micro-channels.

Under the experimental conditions (with same injection flow rate), the mobility of the interfaces was higher within longer micro-channels of the same diameter; within micro-channels of the same length, the interface has a higher mobility in channels with smaller diameters. Different types of introduced fluids also affect the interfaces. As Figure 3-13 demonstrates, the shape of the interfaces varies between the decane-polymer and the De-ionized water-decane, with the former having flatter interfaces and the latter showing a clear meniscus.

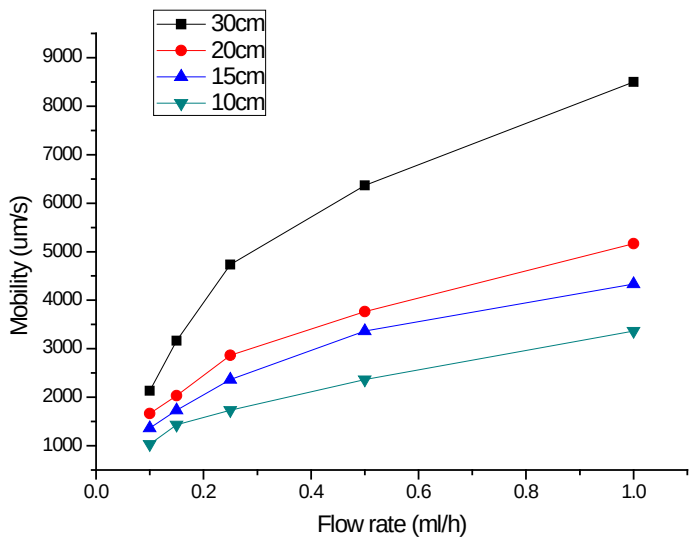

Figure 3-8: Mobility of interfaces with different lengths of capillary tubes (capillary ID = 100um, 0.1%FRW-18)

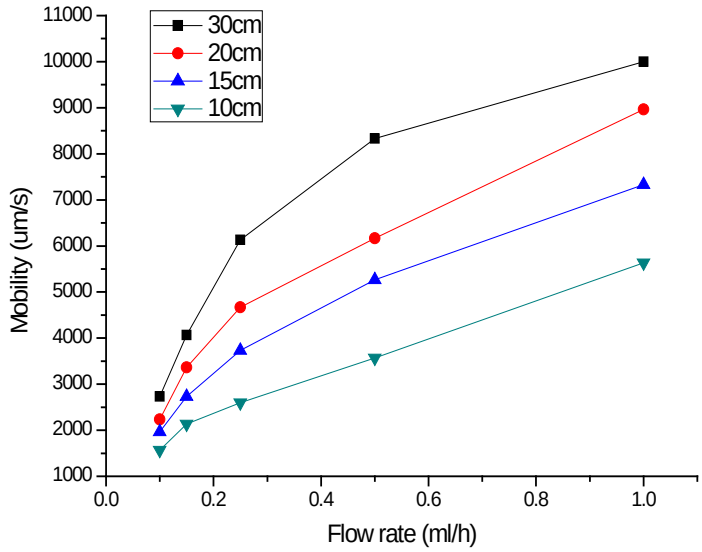

Figure 3-9: Mobility of interfaces with different lengths of capillary tubes (capillary ID = 75 um, 0.1%FRW-18)

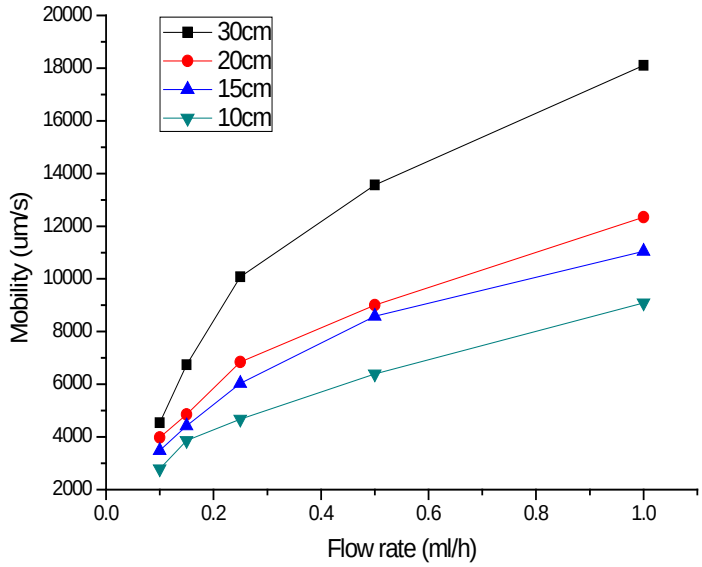

Figure 3-10: Mobility of interfaces with different lengths of capillary tubes (capillary ID = 50um, 0.1%FRW-18)

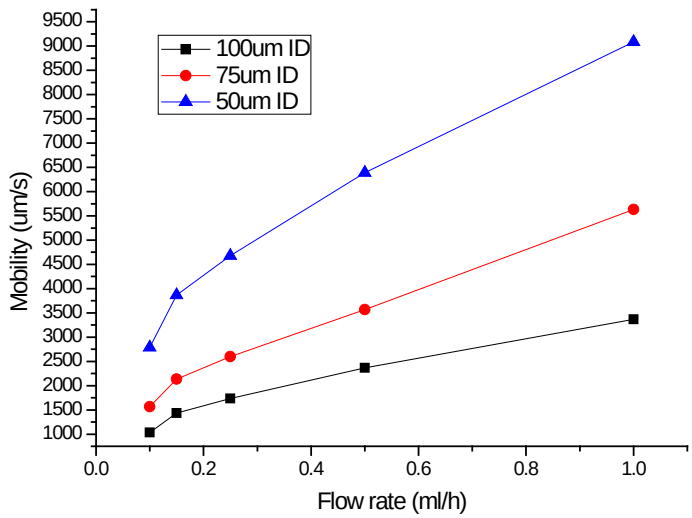

Figure 3-11: Mobility of interfaces with different sizes of capillary tubes (capillary length = 10cm, 0.1%FRW-18)

Figure 3-12 presents the shapes of the interfaces between different liquids. The results indicate that the wettability of the fluids plays an important role in the shapes of the interfaces.

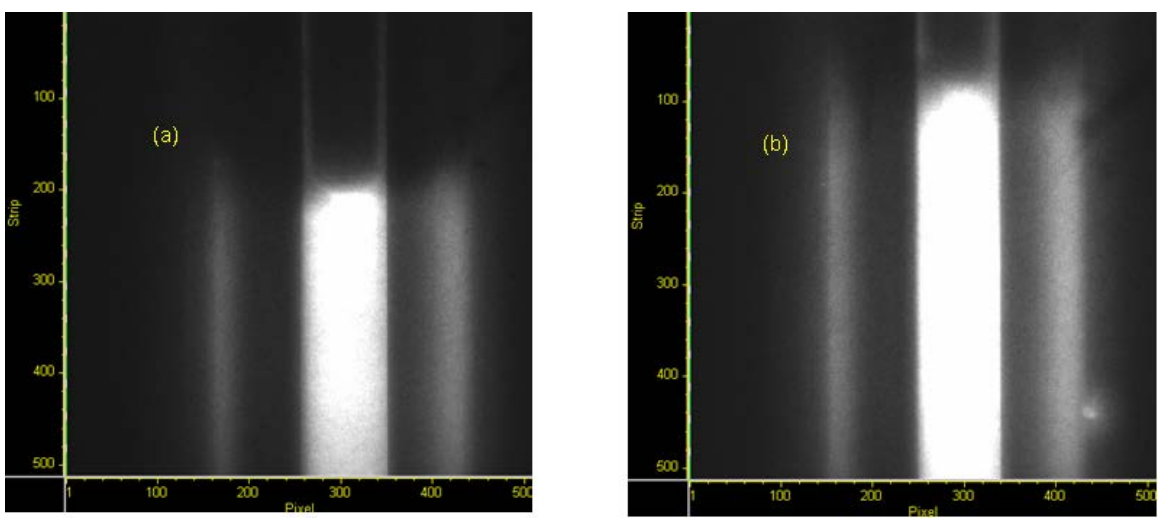

Figure 3-12: Shape of the interfaces: (a) 100um ID capillary, 20x lens, decane push 0.1%FRW-18, d= 5cm ; (b) 100um ID capillary, 20x lens, lab reagent water push 0.1%FRW-18, d= 5cm

3.3.3 Effect of channel size and wettability on the flow behavior of polymer particles

1) Surface wettability and channel sizes of micro-channels

The channel sizes of micro-channels were characterized using an optical microscope. Fig. 3-13 shows the optical microscope images of an unmodified micro-

channel with a hydrophilic inner surface and a modified micro-channel with a hydrophobic inner surface.

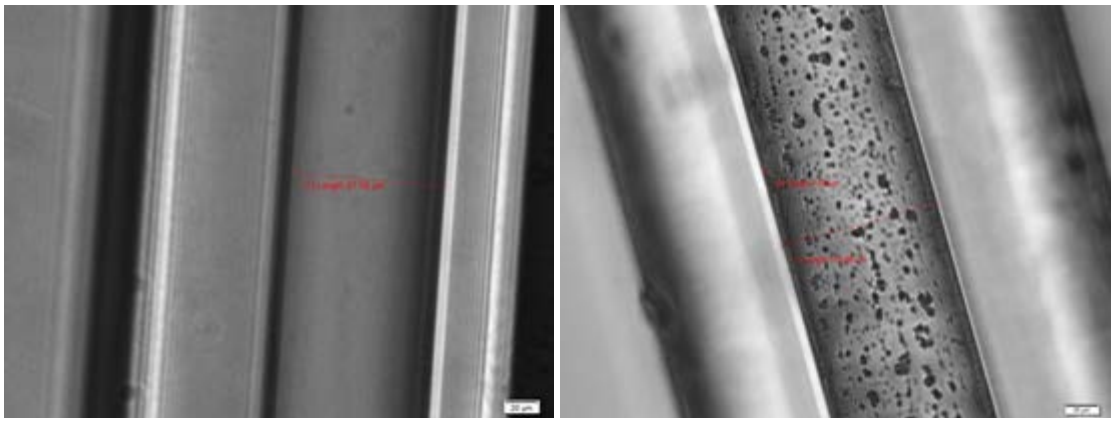

(a) (b)

Figure 3-13: Hydrophilic (a) and hydrophobic (b) inner surface micro-channels

Fig. 3-13a and 3-13b reveal that after being coated with a linear polyacrylamide layer, the inner diameter of the modified micro-channel is almost the same as that of the unmodified micro-channel. Therefore, we can consider the inner radii of modified and unmodified micro-channels to be the same.

We quantify the surface wettability of modified glass micro-channels by measuring water-meniscus heights within the micro-channels, as described in the experimental section. We performed the same measurements for unmodified micro-channels as a blank control for comparison. Fig. 3-14 shows the measured meniscus heights of water in both modified and unmodified micro-channels. The results indicate that hydrophilic and hydrophobic modifications of inner surfaces of micro-channels are successful.

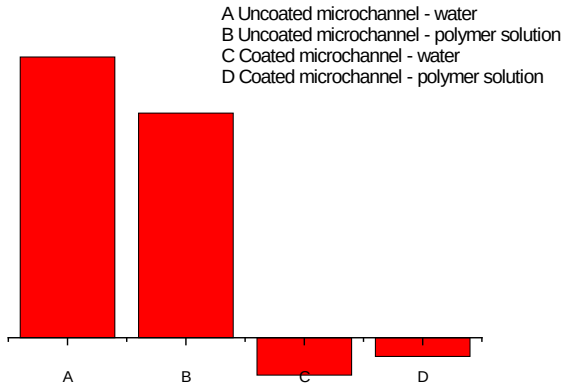

Figure 3-14: Meniscus heights of water in unmodified and modified micro-channels. The minus sign means that the meniscus height inside the micro-channel is lower than the water level outside the micro-channel.

2) Characterization of the FRW-20 polymer: Size distribution and shapes

The size distribution and shapes of the FRW-20 polymer solution were characterized by optical microscope images, as shown in Figure 3-15a. The shapes of polymer particles are spherical, so we refer to them as micro-spheres. The size distribution of the polymer is shown in Figure 3-15b.

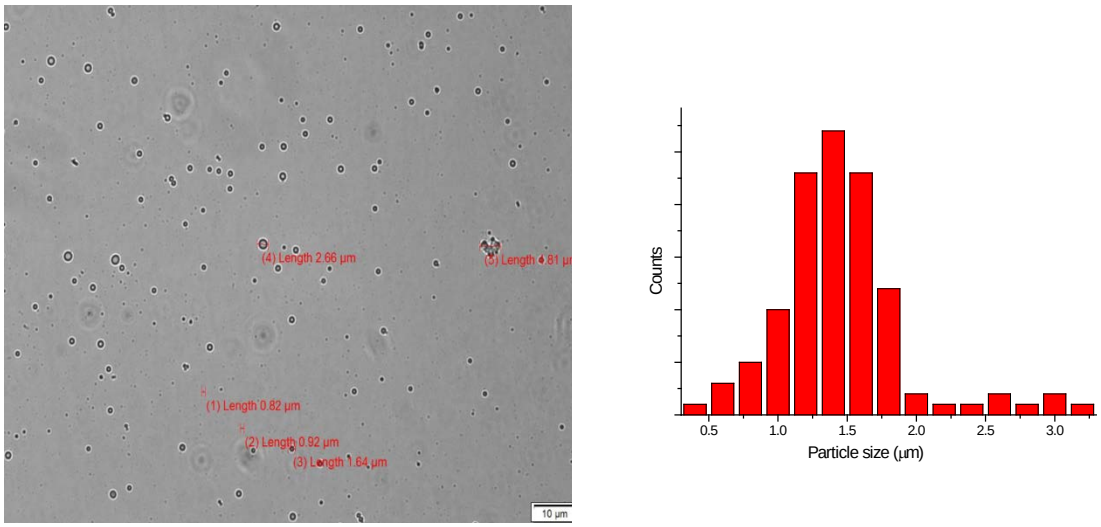

(a) (b)

Figure 3-15: (a) Images of polymer particle FRW-20 (b) Size distribution of polymer particles (FRW-20, 0.1% v/v)

The results show that the sizes of the FRW-20 polymer particles under experimental conditions (0.1% v/v in reagent water) were in the range of 0.5 to 3.4µm, with an average of 1.2 to 1.6µm. This indicates that the polymer micro-spheres are relatively mono-disperse. Compared to the sizes of micro-channels (25µm to 225µm), the sizes of polymer micro-spheres cannot be neglected.

3) Effect of surface wettability and the channel sizes of micro-channels on the aggregation behaviors of polymer micro-spheres

To investigate the effect of surface wettability and the channel size of micro-channels on the aggregation behaviors of polymer micro-spheres, some concentrations of polymer solutions were introduced into each micro-channel. The micro-spheres began to aggregate once the polymer solution was injected. We quantified the number of polymer particles (after aggregation) that passed through the scan window over a certain period of time. The results of the comparison between different channel sizes and wettability conditions, shown in Figure 3-16, indicate that surface wettability does not play a role in aggregation behavior, but the channel size does. In smaller channels, more significant aggregations of polymers were observed.

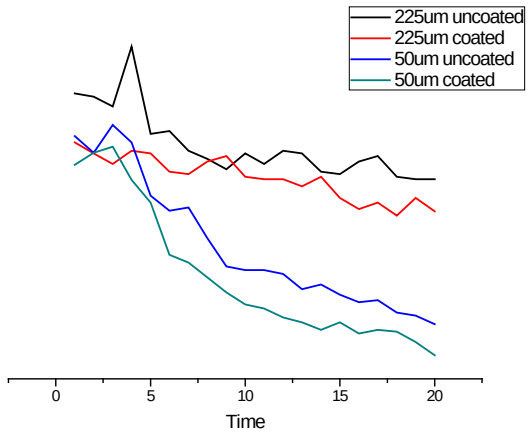

Figure 3-16: Aggregation configuration of FRW-20 under different micro-channel wettability conditions and sizes

4) Effect of surface wettability and the channel sizes of micro-channels on the flow characteristics of FRW-20 micro-spheres

In order to investigate the effect of wettability and channel size on the flow behavior of FRW-20 micro-spheres, the average velocity of each individual polymer micro-sphere was characterized, and the average velocity distribution, along with the Y-axis in the focusing plane, were investigated.

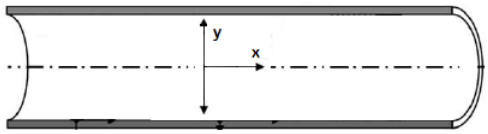

Figure 3-17: Focusing plane

First, the polymer micro-spheres maintained a constant velocity while moving along the direction of the micro-channels. However, their velocities vary with different positions of the polymer micro-spheres in the channels. The velocity distributions of FRW-20 micro-spheres in larger channels with different sizes and wettability conditions have been characterized and are shown in Figure 3-18.

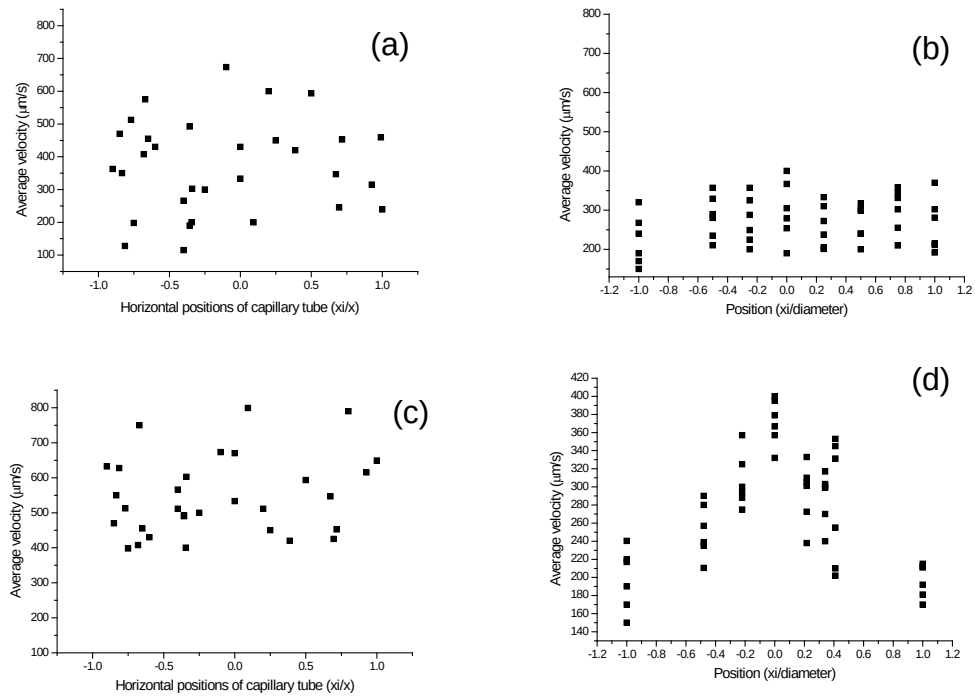

Figure 3-18: The average velocity distribution of FRW-20 in different positions along the Y-axis in micro-channels with different sizes and wettability conditions.

(a) 225μm modified channel; (b) 225μm unmodified channel; (c) 100μm modified channel; (d) 100μm unmodified channel; Four-hundred independent measurements of the micro-sphere velocities in micro-channels are conducted.

In both modified (18a) and unmodified (18b) 225μm channels, the velocities of polymer micro-spheres are generally randomly distributed. There is no correlation between the flow velocities of polymer micro-spheres and their positions in the micro-channels when located from the center to the inner wall. Also, the wettability of the inner surface of the channels does not have a significant influence on the flow velocity distribution; the average flow velocities are almost the same.

In 100μm channels, the velocity distribution of polymer micro-spheres is still random in the modified channel (18c), but in the unmodified channel, the average flow velocities of polymer micro-spheres located in different areas of the channels are different; the polymer micro-spheres located in the center of the channel always have higher flow velocities than those located near the inner wall. A similar phenomenon was observed in smaller diameter channels. Figure 3-20 shows the flow velocity distribution of 50 and 25μm modified and unmodified channels.

With smaller inner diameter channels, the same profiles were observed in unmodified channels; the average flow velocity of the polymer micro-spheres in the center is always higher than of those near the inner wall. However, those profiles are not clearly observed in the modified channels, possibly because the polymer

micro-spheres interact increasingly with the inner wall of the micro-channels when the channel size decreases. The inner surfaces of the channels of unmodified micro-channels are hydrophilic and have the same wettability as the polymer micro-spheres. Thus, when the micro-spheres get close to the inner wall, the adsorption effect between the micro-spheres and the inner wall affects the flow velocity of the micro-spheres. Smaller channel sizes will yield to higher chances that the polymer micro-spheres get close to the inner wall of the channel.

A layer of linear polyacrylamide coating was applied on the inner surface of the modified micro-channels. The wettability of the inner surface has been modified to be hydrophobic, thus suppressing the adsorption of polymer micro-spheres.

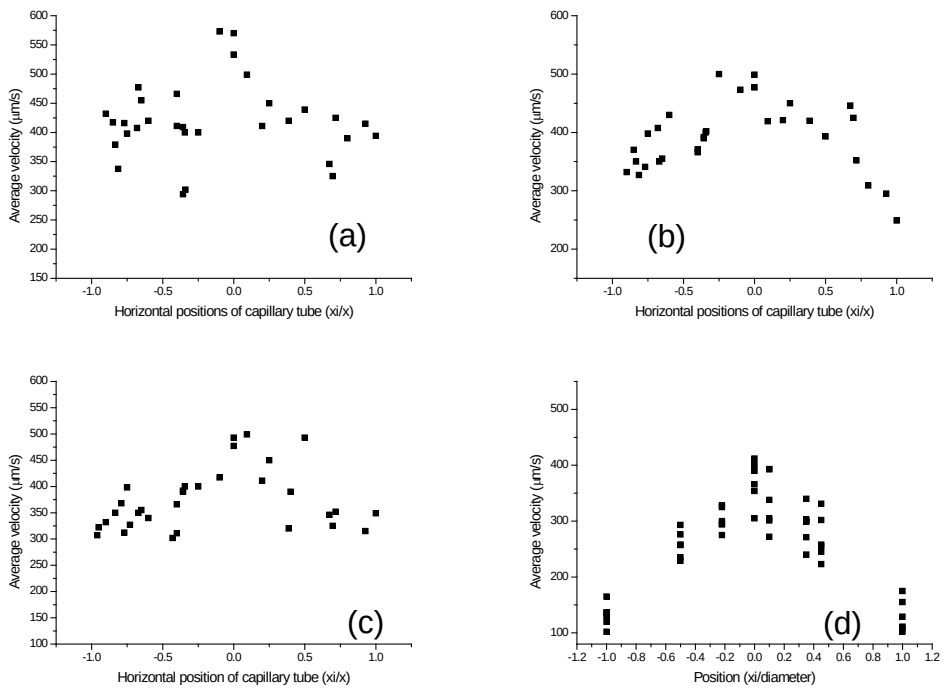

Figure 3-19: The average velocity distribution of FRW-20 in different positions along the Y-axis in micro-channels with different sizes and wettability conditions
(a) 50μm modified channel; (b) 50μm unmodified channel; (c) 25μm modified channel; (d) 25μm unmodified channel; Four-hundred independent measurements of the microsphere velocities in micro-channels are conducted.

3.4 Future work

The flow behavior of gas/introduced fluids in nano-scale channels will be investigated. Detailed information is presented in Part II.

3.5 Conclusions

We systematically investigated the effect of wettability and channel size on fluid flow behavior and aggregation configuration within micro-channels, and gas/fluid

flow profiles were studied in the nano-scale channels. Fused-silica capillary tubes were used as micro-channels, and linear PAM coating was applied to achieve a hydrophobic inner surface. Valuable results regarding the flow characteristics of two fluid interfaces and polymer particles were obtained from a series of systematic experiments. The results showed that the first modification of the surface wettability of a micro-channel was successful. When the channel size decreases, the surface wettability conditions and channel sizes of the microchannels will affect the flow behaviors of polymer particles and the interfaces between the two fluids. Surface modified micro-channels do not have a similar particle velocity distribution profile because the adsorption between the inner wall of the micro-channel and the polymer particles was suppressed. In summary, the results of this study provide valuable information for the application of transfer polymer solutions into different sizes of channels/networks.

Part II. Gas/fluid flow behavior in the nano-channels

3.6 Experimental method

For the gas phase study, high purity nitrogen gas was served as the target gas and was filtered by a 0.22 um gas filter prior to use. Nitric monoxide was used as the gas phase tracer.

Custom-designed and fabricated nano-chips from the Colorado School of Mines were applied to function as sample holders/channels for direct imaging; the chip holder and tubing were designed and built in the workshop to fit the microscope stage.

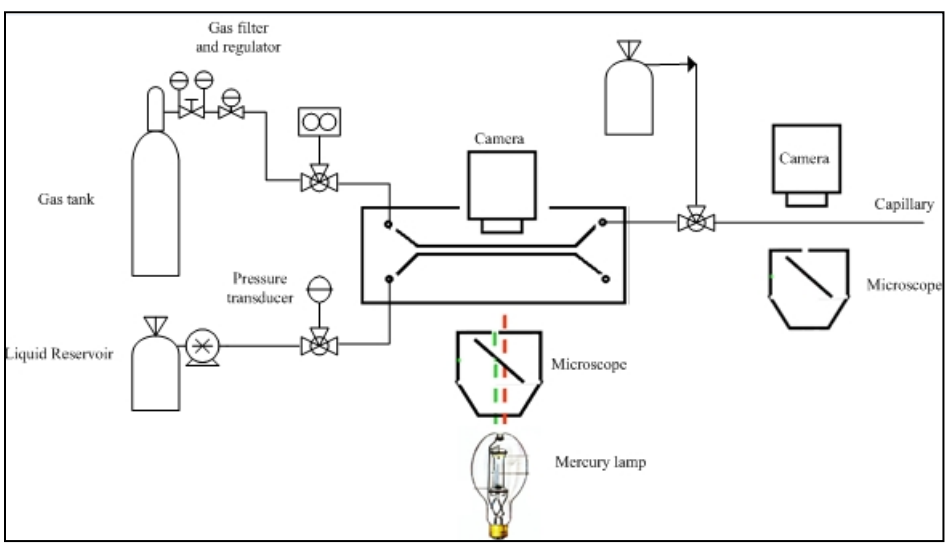

Figure 3-20: Schematic of experimental setup

To study gas visualization, the optic system was adjusted, and a UV range mercury lamp was used to provide an excitation beam. The gain and exposure times of the CCD camera were set at 100ms.

A new fluid transfer system was designed for nano-chips to achieve precise pressure control and online pressure/flow rate measurements while capturing images. The schematic of the system was shown in Figure 3-20. A nitrogen tank was used to supply nitrogen gas, and nitric monoxide was used as a tracer of the gas phase. Fluorescein-labeled solution was introduced into the capillary tube by the syringe pump. The flow behavior of the gas and liquid phase was then captured by the CCD camera. Both the inlet and outlet pressure were monitored by the digital pressure transducer. The liquid displacement method was applied in order to monitor the real-time flow rate of the gas phase. A 2nd camera and microscope were used in this method, and the movement of the gas was recorded by monitoring the interface of the gas/water.

Preliminary tests: Images of the nano-chips

The dimensions of the channels in the nano-chip were tested and measured by the microscope with the CCD camera prior to the fluid behavior study. The images indicate that the dimensions of most channels are well controlled. However, there some roughness exists in the inner wall of the main channel and some of the nano-channels.

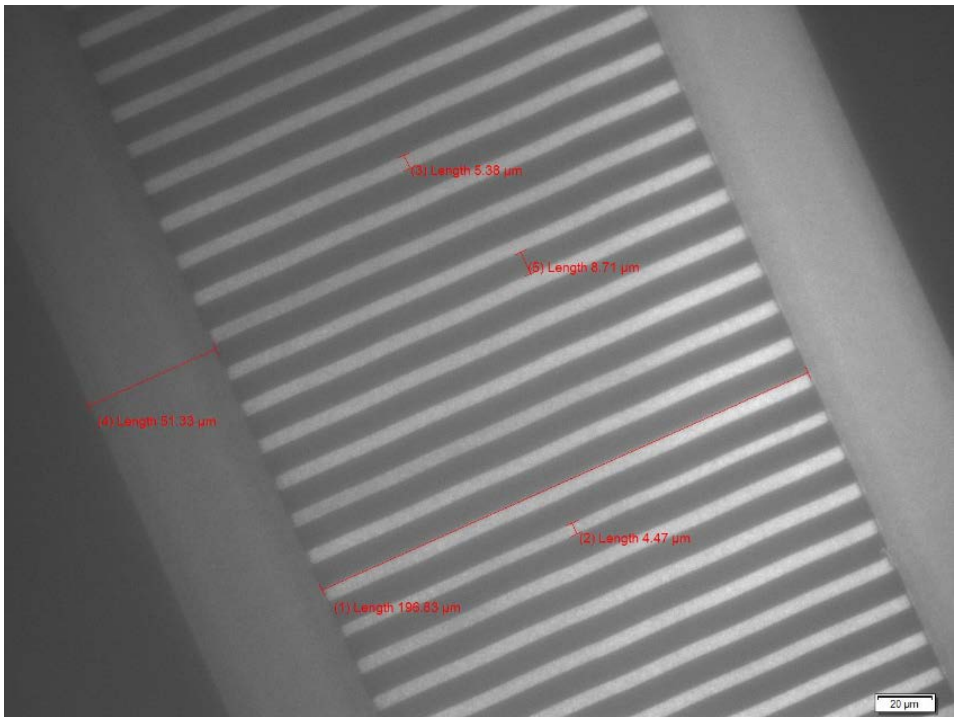

Figure 3-21: Image of the channels of the nano-chips (nano-channels)

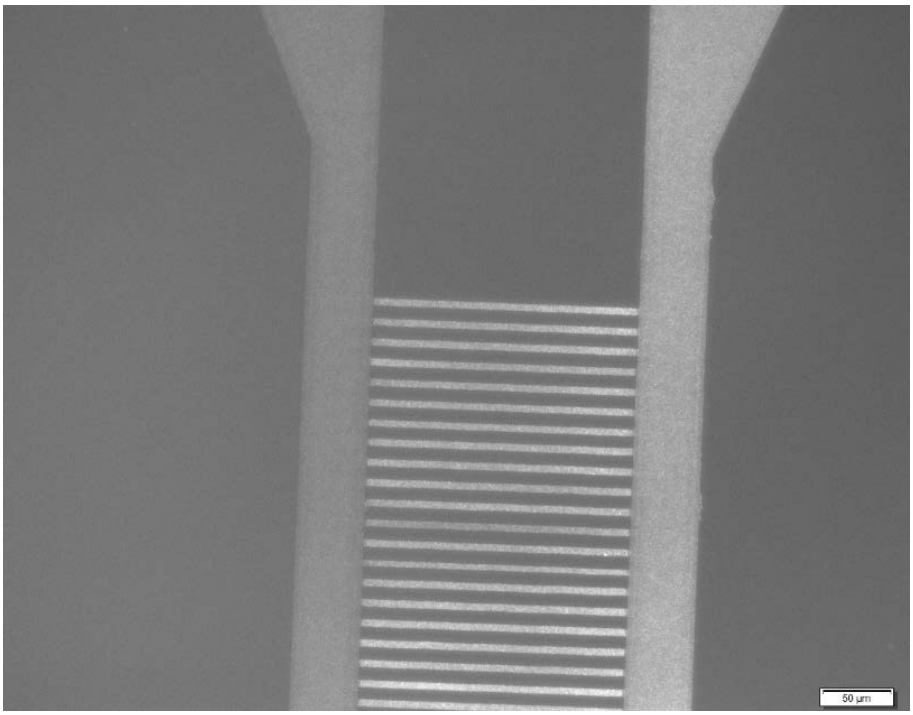

Figure 3-22: Image of the channels of the nano-chips (main channel and nano-channels)

3.7 Future experimental plan

The molecular tagging velocimetry method will be used for gas phase visualization. The experiment's schematic is shown in Figure 3-23. A mercury lamp will be used for the light source, and the wavelength of the excitation beam will be set at 225nm by a band pass filter. The emission light will be captured by the CCD camera equipped with a long-pass filter.

High-purity nitrogen gas with nitric monoxide will be delivered into the channel first. Nitric monoxide will be excited by the UV light from the mercury lamp at a wavelength of 225nm and will emit visible light. Then, the image will be captured by the high-speed camera. The flow profile, real-time diffusion process and sorption (if it occurred) will be characterized.

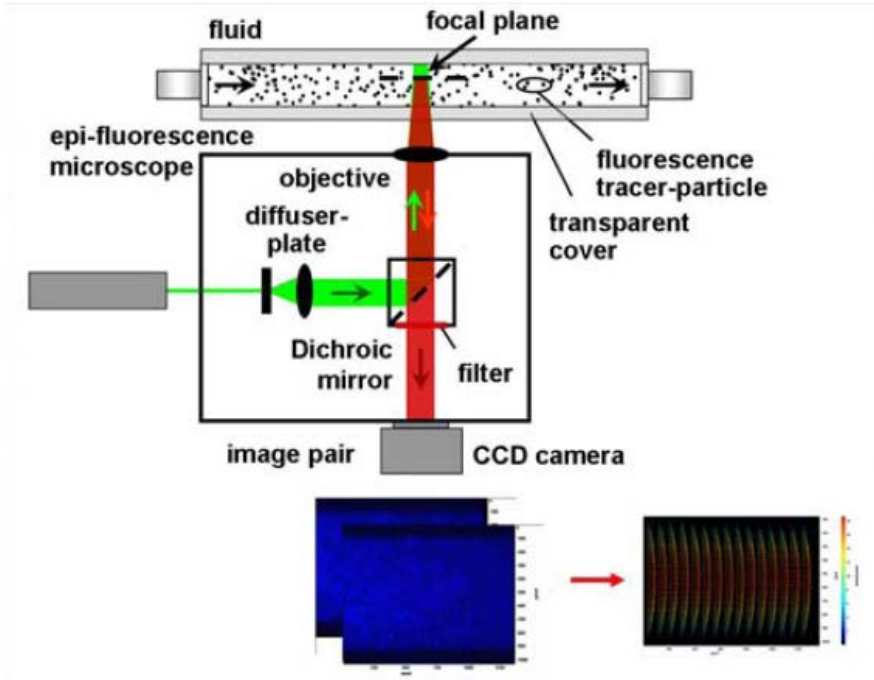

Figure 3-23: Schematic of epi-fluorescence system for molecular tagging velocimetry method

3.8 Review: Published study of gas flow behavior in micro-/nano-channels

Many experimental studies have been conducted in order to analyze the behavior of convection through micro-channels, and a review is available in [23-25, 29]. This section will summarize the results of these previous publications. First, the main goal of these studies was to determine the friction factors and the convective heat transfer coefficients through micro-channels in which a pressure-driven flow was imposed.

Over the past few years, improvements in micro-fabrication techniques have enabled more accurate control over the geometry of micro-/nano-channels, and innovative, more accurate measurement techniques for micro-flows have been proposed with a general improvement of the reliability/accuracy of the experimental data reported in the literature. These most recent data seem to agree well with classical theory. This highlights the need for the development of specific measurement techniques in the micro-fluidics field or a refinement and adaption of the ones used at larger scales.

There is a very urgent need for the development of specific measurement techniques in the field of micro-fluidics. Different approaches for measuring the main operative parameters useful in determining the friction factors and pressure drops through micro-channels (such as micro-channel size, pressure, temperature and gas flow rate) will be presented, highlighting both the advantages and possible problems.

Estimating the Average Inner Diameter of a Micro-channel: The method of accumulating heavy liquid proposed by Asako et al. [26] seems to work well for reducing the uncertainty accompanying this measurement (<0.2%). This technique is based on the assumption that the Poiseuille law for liquid flows in the laminar regime holds true in micro-channels, as well. However, for very small hydraulic diameters, this technique requires a very long time for the liquid to accumulate; when water is used as the test fluid, care must be used when estimating the mass lost due to evaporation during the experimental tests, which strongly depends on the environmental conditions.

Estimating the Flow Rate: Commercial thermal mass flow sensors can be used down to 108 kg/s (0.1 Nml/min). When the mass flow rate is very low ($<10^{-8}$ kg/s), the best method is the single-tank constant volume method proposed by Ewart et al. [27] and, more recently, the same method with double measurement and precise temperature regulation proposed by Pitakarnnop et al. [28]. During measurement, the environmental conditions must be checked accurately in order to maintain a constant temperature.

Determining the Pressure in a Micro-channel: It is possible to reconstruct the pressure distribution along a micro-channel, but doing so requires specific techniques and sensors (pressure-sensitive paints, micro-strain gauge membrane, optical lever), which further require a specific calibration and sometimes a specific test section. If the only value of interest is the total pressure drop along a micro-tube, normal pressure sensors can be used. These devices can be employed with low levels of relative uncertainty (<±0.5%) by placing them in the plenums at the inlet and outlet of the micro-channel. However, in this case, correctly evaluating the minor losses at the ends of the micro-tube becomes crucial. In addition, for compressible and incompressible flows, different pressure measurement strategies (i.e., the combination of absolute and differential pressure sensors) may result in variable accuracy of the friction factor.

Temperature: Thermocouples, thermal liquid crystals or infrared thermography can be used to estimate the surface temperature of the micro-devices; in general, however, the use of classical Pt-RTD sensors and thermocouples is usually recommended in order to determine the temperature in micro-fluidic devices. However, this paper showed that improvements in micro-fabrication techniques has led to the realization of specific μRTD, TFTC and SC micro-sensors, and their integration in micro-channels has been demonstrated to be very promising for analyzing gas dynamics in micro-channels.

Determining the Local Velocity Distribution: The velocimetry techniques proposed for liquid flows in micro-channels present strong limitations if applied to the analysis of gas flows. To determine the local velocity of a gas in a micro-channel, two techniques have been proposed: micro-Particle Image Velocimetry (μPIV) and Molecular-Tagging Velocimetry (MTV). For μPIV, the accuracy of the gas-phase flow velocity measurement is strongly dependent on the characteristics of the tracer

particles; it has been demonstrated that for gas flows through micro-channels, the seeding (water or fluorescent oil) must be characterized by diameters below 1 um in order to closely follow the flow, especially in regions of rapid deceleration (bends). This can cause serious problems for the generation of the tracer particles, especially for low gas flow rates. On the other hand, the application of MTV to the analysis of gas flows through micro-channels is only in its preliminary phase. Determining the local velocity in micro-devices remains an important open question.

Visualizing the Gas-Phase Flow: Gas-phase PIV measurements used in millimeter-channels were reported by a few groups and research institutes. All of them used light sheet illumination and measured transparent model channels in non-operational conditions. Grega and McGarry [30] performed detailed flow measurements through a scaled plexi-glass model of a fuel cell stack using PIV. The flow was seeded with an oil-based aerosol in the air with nominal particle diameters of 1μm. Using the PIV technique, instantaneous flow fields were captured and then averaged to obtain mean values and velocity statistics. Based on these data, relationships were found between manifold and cell flow distributions. Sugii and Okamoto [31] used the micro-PIV technique to investigate the flow in a transparent model of a polymer electrolyte fuel cell under non-operational conditions, which consisted of straight 1mm channels. The velocity distribution of the gas flow with Reynolds numbers of 26 and 130 were measured successfully. Yoon et al. [32] measured gas phase velocity fields using particle image velocimetry in acrylic millimeter-scale channels with integrated heaters and in a PDMS 180° switchback flow model.

4. Numerical simulation

4.1 Introduction

The objective of Task 7 is to develop a multiphase flow numerical model to simulate the invasion of hydraulic fracturing fluid into nano-pores and the flowback driven by formation pressure. The three milestones associated with Task 7 are:

a) Development of a parallelized, 3D lattice Boltzmann simulator capable of simulating multiphase flows (End of Year 1);
b) Implementation of a transport module in the simulator (End of Year 2);
c) Implementation of a particle to simulate the effect of polymer or nano-particle additives on fluid flow (End of Year 3).

In the past eight months, we have met the Year 1 milestone. Specifically, we successfully developed a three-dimensional, parallelized, multi-fluid lattice Boltzmann simulator. This simulator can use real porous media images obtained from micro-computed tomography (micro-CT) or a focused ion beam (FIB)–scanning electronic microscope (SEM) as input parameters. Alternatively, the simulator also can employ synthetic geometry models. The results obtained from single-phase flow simulations agreed well with existing and new experimental and numerical data. A Shan-Chen two-phase lattice Boltzmann model was used to test the implementation of fluid-fluid interfacial tension and fluid-solid-fluid contact angle. Multiphase flow simulation has not been conducted but is underway.

4.2 Methods

Synthetic Geometry Models: We developed several types of synthetic geometry models to study the fundamental correlation between porous media geometry and permeability. In the study of porous media flow and transport, synthetic geometry models are useful when the actual pore geometry is unavailable or difficult to measure. Due to the prevalence of nano-scale features in tight gas sands and shale, directly measuring pore structure is difficult, and synthetic geometries that match the bulk properties of the rock (e.g., porosity, permeability) can be used, as well as controlled first-order approximations. Flow correlations established for idealized, synthetic geometries also provide important bounds for understanding the flow behavior in real rocks; deviations from idealized behaviors can be used to back-calculate or project the structure of real rocks.

Our synthetic two- and three-dimensional geometries all are built from Voronoi diagrams. The Voronoi diagram is a well-established mathematical method [33] that, starting from a set of randomly-distributed points (Poisson points), divides a two-dimensional or three-dimensional domain into many non-overlapping polygons (2D) or polyhedrons (3D). Voronoi diagrams can be applied to a wide range of applications, including nearest neighbor inquiries, unstructured mesh generation,

and connectivity and percolation networks [34]. Many numerical and theoretical studies on porous media flow and transport have used Voronoi geometries to approximate pore networks [35] or to construct actual pore spaces [36]. Here, we used Fig. 4-1 to illustrate our procedure of using the edges of a 2D Voronoi diagram to create a fully-percolated pore network.

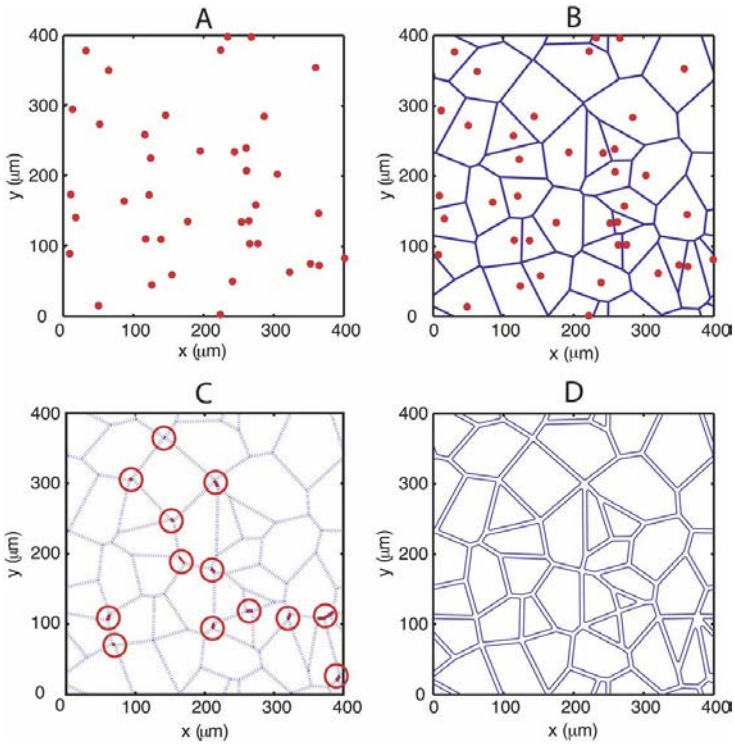

Figure 4-1: Generation of a fully-percolated pore network from a 2D Voronoi diagram.
A) A collection of Poisson points is generated; B) A Voronoi diagram is generated from the Poisson points (coordination number = 3); C) Short edges are removed, and the coordination number is perturbed; D) The edges of the Voronoi diagram are given a finite width, and a network of channels is created. In this example, all channels have the same width.

The above procedures generate an idealized pore network composed of identically-sized channels. In real porous media, the pore structure is very different from a network of channels of the same size. Perturbations to the network can be achieved by 1) using a non-uniform distribution of Poisson points; 2) introducing a distribution of channel widths; and 3) randomly removing individual grains or clusters of grains to generate large isolated pores known as vugs. These perturbations generate better approximations of real porous media (Fig. 4-2a-b).

Three-dimensional synthetic geometries can be generated in a similar fashion. Specifically, if the edges of three-dimensional Voronoi diagrams are turned into capillary tubes, a porous medium consisting of randomly-distributed and interconnected capillary tubes is generated (Fig. 4-2d). Alternatively, if the faces of Voronoi polyhedrons are given a finite width, pore space in the form of interconnected fractures is generated (Fig. 4-2c). The tubular geometry also can be inverted to create a fibrous network.

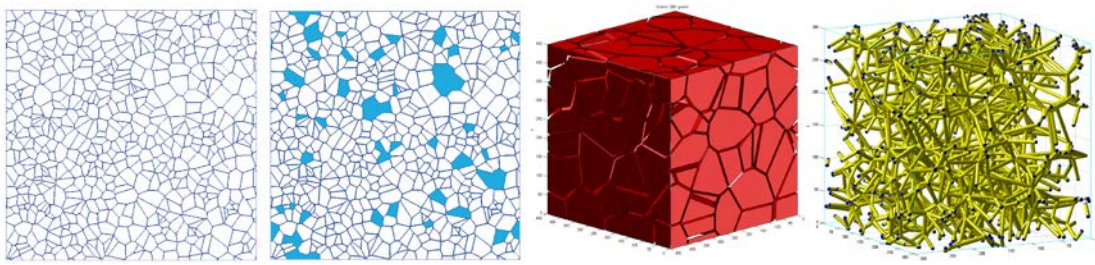

Figure 4-2: Synthetic porous media geometries for flow simulations.
From left to right: a) Homogeneous synthetic 2D porous media model composed of networks of channels; b) Heterogeneous synthetic 2D porous media model composed of channels and vugs; c) 3D synthetic porous media model with polyhedron grains surrounded by interconnected fractures; d) 3D synthetic porous media model with interconnected tubular (or fibrous) structure.

Lattice Boltzmann Method for Fluid Flow: Unlike finite difference, finite volume, or finite element methods, the lattice Boltzmann method solves the Navier-Stokes equation indirectly by simulating the evolution of a simplified fluid molecular velocity distribution function on a space-filling cubic lattice. The simplified distributions used in this study contain 9 discrete velocities for 2D simulations (D2Q9) and 19 velocities for 3D simulations (D3Q19). For the D2Q9 model, the discrete velocities are along the [00] (stationary), [10] (axial), and [11] (diagonal) directions. For the D3Q19 model, the discrete velocities include the [000] (stationary), [100] (axial), and [110] (diagonals on coordinate planes) directions. Such a design ensures that the molecules arrive at a lattice node in only one time step.

The fraction of molecules traveling in the direction of discrete velocity $\mathbf{c}_i$ is n_i. The fluid density, momentum, and stress are the zeroth, first, and second order moments of n_i over the velocity space:

$$\sum_i n_i = \rho \qquad \sum_i n_i \mathbf{c}_i = \rho \mathbf{u} \qquad \sum_i n_i \mathbf{c}_i \mathbf{c}_i = \mathbf{\Pi}\,.$$

In the lattice Boltzmann method, n_i is updated by the following equation:

$$n_i\left(\mathbf{r}_j + \mathbf{c}_i \Delta t, t + \Delta t\right) = n_i\left(\mathbf{r}, t\right) + \Omega_i\left(\mathbf{n}\left(\mathbf{r}, t\right)\right)$$

where $\Omega_i\left(\mathbf{n}\left(\mathbf{r}, t\right)\right)$ models a local molecular collision process that relaxes the non-equilibrium part of n_i toward equilibrium. After collisions take place, according to the evolution equation, the post-collision distributions $n_i\left(\mathbf{r}, t\right) + \Omega_i\left(\mathbf{n}\left(\mathbf{r}, t\right)\right)$ are sent to the lattice node in the direction of $\mathbf{c}_i$; this process is called propagation or advection. In this study, we used the MRT (multi-relaxation-time) collision scheme developed by Lallemand and Luo [37] and d'Humières [38], which has three steps. On the D2Q9 lattice (two-dimensional), first the kinetic moment vector ξ is calculated from the pre-collision molecular velocity distribution vector $\mathbf{n} = \left[n_1, \cdots, n_9\right]$

$$\xi = \lfloor \rho, e, \varepsilon, j_x, j_y, q_x, q_y, p_{xx}, p_{xy} \rfloor = \mathbf{M} \cdot \mathbf{n}$$

where **M** is a 9-by-9 square matrix

$$\mathbf{M} = \begin{bmatrix} 1 & 1 & 1 & 1 & 1 & 1 & 1 & 1 & 1 \\ -4 & -1 & -1 & -1 & -1 & 2 & 2 & 2 & 2 \\ 4 & -2 & -2 & -2 & -2 & 1 & 1 & 1 & 1 \\ 0 & 1 & -1 & 0 & 0 & 1 & 1 & -1 & -1 \\ 0 & -2 & 2 & 0 & 0 & 1 & 1 & -1 & -1 \\ 0 & 0 & 0 & 1 & -1 & 1 & -1 & 1 & -1 \\ 0 & 0 & 0 & -2 & 2 & 1 & -1 & 1 & -1 \\ 0 & 1 & 1 & -1 & -1 & 0 & 0 & 0 & 0 \\ 0 & 0 & 0 & 0 & 0 & 1 & -1 & -1 & 1 \end{bmatrix}$$

The kinetic moment vector ξ is then relaxed to ξ* based on the following equations:

$$\xi^* = \left[\rho, e^*, \varepsilon^*, j_x, q_x^*, j_y, q_y^*, p_{xx}^*, p_{xy}^*\right]$$

$$\begin{aligned}
e^{eq} &= -2\rho + \frac{3\left(j_x^2 + j_y^2\right)}{\rho_0} & e^* &= e - s_2\left(e - e^{eq}\right) \\
\varepsilon^{eq} &= \rho - \frac{3\left(j_x^2 + j_y^2\right)}{\rho_0} & \varepsilon^* &= \varepsilon - s_3\left(\varepsilon - \varepsilon^{eq}\right) \\
q_x^{eq} &= -j_x & q_x^* &= q_y - s_5\left(q_x - q_x^{eq}\right) \\
q_y^{eq} &= -j_y & q_y^* &= q_y - s_7\left(q_y - q_y^{eq}\right) \\
p_{xx}^{eq} &= \frac{j_x^2 - j_y^2}{3\rho_0} & p_{xx}^* &= p_{xx} - s_8\left(p_{xx} - p_{xx}^{eq}\right) \\
p_{xy}^{eq} &= \frac{j_x j_y}{3\rho_0} & p_{xy}^* &= p_{xy} - s_9\left(p_{xy} - p_{xy}^{eq}\right)
\end{aligned}$$

$$s_2 = s_3 = s_8 = s_9 = \frac{1}{\tau}$$

$$s_5 = s_7 = 8\frac{2 - s_2}{8 - s_2}$$

Finally, Ω_i is calculated using $\Omega_i = \mathbf{M}^{-1} \cdot \boldsymbol{\xi}^*$.

The MRT scheme for the D3Q19 model is similar to that for the D2Q9 model, except that the kinetic moment vector contains 19 elements:

$$\xi = \lfloor \rho, e, \varepsilon, j_x, q_x, j_y, q_y, j_z, q_z, 3p_{xx}, 3\pi_{xx}, p_{ww}, \pi_{ww}, p_{xy}, p_{yz}, p_{zx}, m_x, m_y, m_z \rfloor = \mathbf{M} \cdot \mathbf{n}$$

and the matrix **M** is 19-by-19 in size:

$$
\mathbf{M} = \begin{bmatrix}
1 & 1 & 1 & 1 & 1 & 1 & 1 & 1 & 1 & 1 & 1 & 1 & 1 & 1 & 1 & 1 & 1 & 1 & 1 \\
-30 & -11 & -11 & -11 & -11 & -11 & -11 & 8 & 8 & 8 & 8 & 8 & 8 & 8 & 8 & 8 & 8 & 8 & 8 \\
12 & -4 & -4 & -4 & -4 & -4 & -4 & 1 & 1 & 1 & 1 & 1 & 1 & 1 & 1 & 1 & 1 & 1 & 1 \\
0 & 1 & -1 & 0 & 0 & 0 & 0 & 1 & -1 & 1 & -1 & 1 & -1 & 1 & -1 & 0 & 0 & 0 & 0 \\
0 & -4 & 4 & 0 & 0 & 0 & 0 & 1 & -1 & 1 & -1 & 1 & -1 & 1 & -1 & 0 & 0 & 0 & 0 \\
0 & 0 & 0 & 1 & -1 & 0 & 0 & 1 & 1 & -1 & -1 & 0 & 0 & 0 & 0 & 1 & -1 & 1 & -1 \\
0 & 0 & 0 & -4 & 4 & 0 & 0 & 1 & 1 & -1 & -1 & 0 & 0 & 0 & 0 & 1 & -1 & 1 & -1 \\
0 & 0 & 0 & 0 & 0 & 1 & -1 & 0 & 0 & 0 & 0 & 1 & 1 & -1 & -1 & 1 & 1 & -1 & -1 \\
0 & 0 & 0 & 0 & 0 & -4 & 4 & 0 & 0 & 0 & 0 & 1 & 1 & -1 & -1 & 1 & 1 & -1 & -1 \\
0 & 2 & 2 & -1 & -1 & -1 & -1 & 1 & 1 & 1 & 1 & 1 & 1 & 1 & 1 & -2 & -2 & -2 & -2 \\
0 & -4 & -4 & 2 & 2 & 2 & 2 & 1 & 1 & 1 & 1 & 1 & 1 & 1 & 1 & -2 & -2 & -2 & -2 \\
0 & 0 & 0 & 1 & 1 & -1 & -1 & 1 & 1 & 1 & 1 & -1 & -1 & -1 & -1 & 0 & 0 & 0 & 0 \\
0 & 0 & 0 & -2 & -2 & 2 & 2 & 1 & 1 & 1 & 1 & -1 & -1 & -1 & -1 & 0 & 0 & 0 & 0 \\
0 & 0 & 0 & 0 & 0 & 0 & 0 & 1 & -1 & -1 & 1 & 0 & 0 & 0 & 0 & 0 & 0 & 0 & 0 \\
0 & 0 & 0 & 0 & 0 & 0 & 0 & 0 & 0 & 0 & 0 & 0 & 0 & 0 & 0 & 1 & -1 & -1 & 1 \\
0 & 0 & 0 & 0 & 0 & 0 & 0 & 0 & 0 & 0 & 0 & 1 & -1 & -1 & 1 & 0 & 0 & 0 & 0 \\
0 & 0 & 0 & 0 & 0 & 0 & 0 & 1 & -1 & 1 & -1 & -1 & 1 & -1 & 1 & 0 & 0 & 0 & 0 \\
0 & 0 & 0 & 0 & 0 & 0 & 0 & -1 & -1 & 1 & 1 & 0 & 0 & 0 & 0 & 1 & -1 & 1 & -1 \\
0 & 0 & 0 & 0 & 0 & 0 & 0 & 0 & 0 & 0 & 0 & 1 & 1 & -1 & -1 & -1 & -1 & 1 & 1
\end{bmatrix}
$$

Relaxation of the kinetic moment vector is calculated based on the following equations:

$$
\xi^* = \left[\rho, e^*, \varepsilon^*, j_x, q_x^*, j_y, q_y^*, j_z, q_z^*, 3p_{xx}^*, 3\pi_{xx}^*, p_{ww}^*, \pi_{ww}^*, p_{xy}^*, p_{yz}^*, p_{zx}^*, m_x^*, m_y^*, m_z^*\right]
$$

$$
\begin{aligned}
e^{eq} &= -11\rho + \frac{19}{\rho_0}\left(j_x^2 + j_y^2 + j_z^2\right) & e^* &= e - s_1\left(e - e^{eq}\right) \\
\varepsilon^{eq} &= 3\rho - \frac{11}{2\rho_0}\left(j_x^2 + j_y^2 + j_z^2\right) & \varepsilon^* &= \varepsilon - s_2\left(\varepsilon - \varepsilon^{eq}\right) \\
q_x^{eq} &= -\frac{2}{3} j_x & q_x^* &= q_x - s_4\left(q_x - q_x^{eq}\right) \\
q_y^{eq} &= -\frac{2}{3} j_y & q_y^* &= q_y - s_4\left(q_y - q_y^{eq}\right) \\
q_z^{eq} &= -\frac{2}{3} j_z & q_z^* &= q_z - s_4\left(q_z - q_z^{eq}\right) \\
p_{xx}^{eq} &= \frac{1}{3\rho_0}\left(2j_x^2 - j_y^2 - j_z^2\right) & p_{xx}^* &= p_{xz} - s_9\left(p_{xz} - p_{xz}^{eq}\right) \\
\pi_{xx}^{eq} &= -\frac{1}{2} p_{xx}^{eq} & \pi_{xx}^* &= \pi_{xz} - s_{10}\left(\pi_{xz} - \pi_{xz}^{eq}\right) \\
p_{ww}^{eq} &= \frac{1}{\rho_0}\left(j_y^2 - j_z^2\right) & p_{ww}^* &= p_{ww} - s_9\left(p_{ww} - p_{ww}^{eq}\right) \\
\pi_{ww}^{eq} &= -\frac{1}{2} p_{ww}^{eq} & \pi_{ww}^* &= \pi_{ww} - s_{10}\left(\pi_{ww} - \pi_{ww}^{eq}\right) \\
p_{xy}^{eq} &= \frac{1}{\rho_0} j_x j_y & p_{xy}^* &= p_{xy} - s_{13}\left(p_{xy} - p_{xy}^{eq}\right) \\
p_{yz}^{eq} &= \frac{1}{\rho_0} j_y j_z & p_{yz}^* &= p_{yz} - s_{13}\left(p_{yz} - p_{yz}^{eq}\right) \\
p_{zx}^{eq} &= \frac{1}{\rho_0} j_z j_x & p_{zx}^* &= p_{zx} - s_{13}\left(p_{zx} - p_{zx}^{eq}\right) \\
m_x^{eq} &= 0 & m_x^* &= m_x - s_{16}\left(m_x - m_x^{eq}\right) \\
m_y^{eq} &= 0 & m_y^* &= m_y - s_{16}\left(m_y - m_y^{eq}\right) \\
m_z^{eq} &= 0 & m_z^* &= m_z - s_{16}\left(m_z - m_z^{eq}\right)
\end{aligned}
$$

$$
\begin{aligned}
& s_1 = s_2 = s_9 = s_{10} = s_{13} = s_{16} = \tau \\
& s_4 = 8\frac{2 - s_2}{8 - s_2}
\end{aligned}
$$

and $\Omega_i = \mathbf{M}^{-1} \cdot \boldsymbol{\xi}^*$.

The static density of the lattice fluid $\rho_0 = 36$ and the viscosity of the lattice fluid is:

$$\mu = \rho_0 c_s^2 \left(\tau - \frac{1}{2}\right)$$

where $c_s^2 = 1/3$ is the square of the speed of sound of the lattice fluid.

After the post-collision populations $n_i(\mathbf{r}, t) + \Omega_i$ are calculated, they are propagated on the lattice based on velocity $\mathbf{c}_i$. If propagation causes a population to cross a fluid-solid boundary, it is bounced back to the original node. This treatment recovers the no-slip boundary condition on a solid wall.

Parallelization and Implementation of Multiple Fluids: The lattice Boltzmann method is parallelized using MPI. The computational domain is divided into 2^n sub-domains, and each sub-domain is assigned to a processor or thread. In every time step, a processor calculates the collision step $n_i(\mathbf{r},t)+\Omega_i$ and then propagates the post-collision distributions. Populations that will be propagated to other sub-domains are stored in a buffer. After a collision-propagation cycle is completed on every processor, a communication step is programmed so that populations stored in the buffer reach their respective destination sub-domains.

When multiple fluid components are present, the program first computes the interactive forces among the components and then conducts collision and propagation component by component.

The parallelized lattice Boltzmann framework can use synthetic geometries or three-dimensional images of rocks obtained from computed tomography as input. Fig. 4-3 shows its flow diagram.

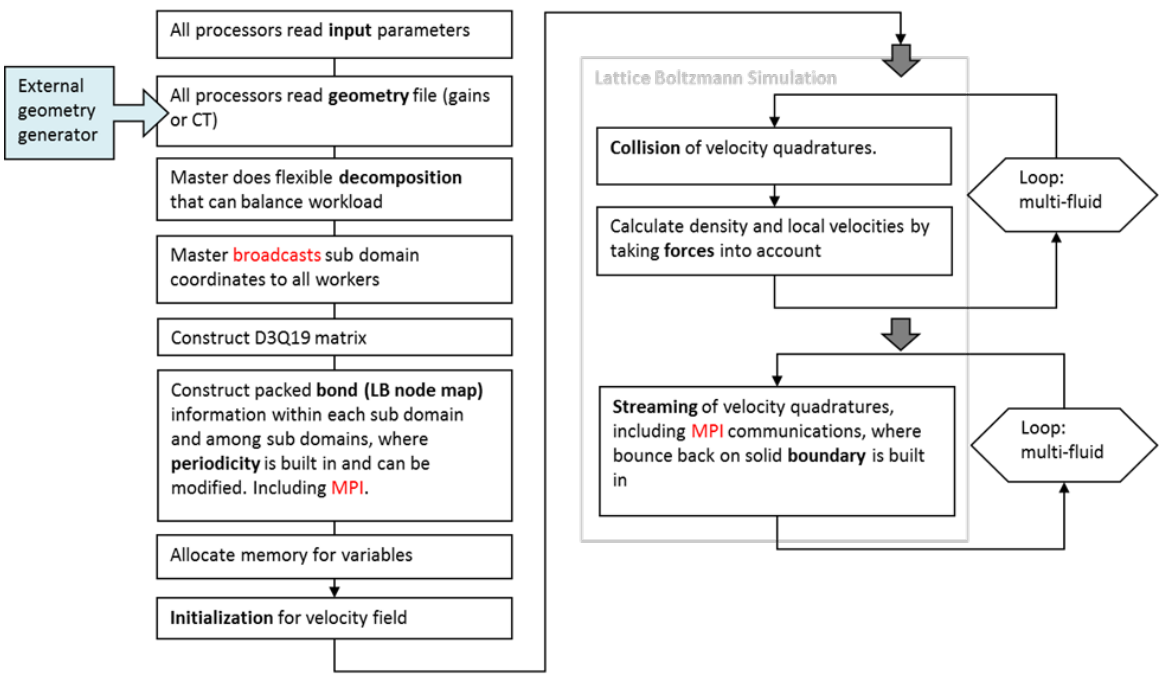

Figure 4-3: Flow diagram of three-dimensional, parallelized lattice Boltzmann multi-fluid simulator.

4.3 Results and Discussions

Parallel Speedup of the Lattice Boltzmann Multi-Fluid Simulator: When tested on RA – the computer cluster on campus (Colorado School of Mines) - the simulator achieved nearly ideal parallel speedup (Fig. 4-4). To date, the largest system simulated contained more than 1000^3 solid and fluid voxels. This development allows us to simulate three-dimensional porous media flow on a meaningful scale.

Direct simulation of fluid flow in micro- and nano-fluidic networks and flow in real porous media geometries obtained from three-dimensional imaging is now feasible.

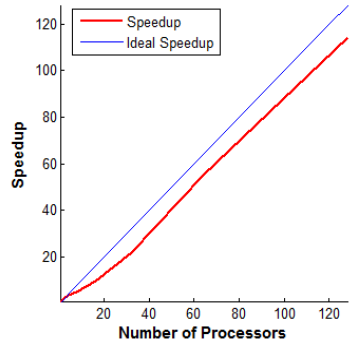

Figure 4-4: Parallel speedup of 3D single-phase lattice Boltzmann simulator.
The test is conducted on a porous system with 80^3 lattice nodes, of which 75% are occupied by pore fluid.

Simulation of Single- and Two-Phase Flow: In our recently published paper [40], the permeabilities of micro-fluidic porous networks obtained from the parallelized lattice Boltzmann simulator agreed very well with experimental measurements. In addition, we also simulated flows through three types of ideal synthetic geometries (granular with fractures, tubular, and fibrous). The porosity-permeability relations obtained for those geometries agreed well with existing correlations and numerical data (Fig. 4-5).

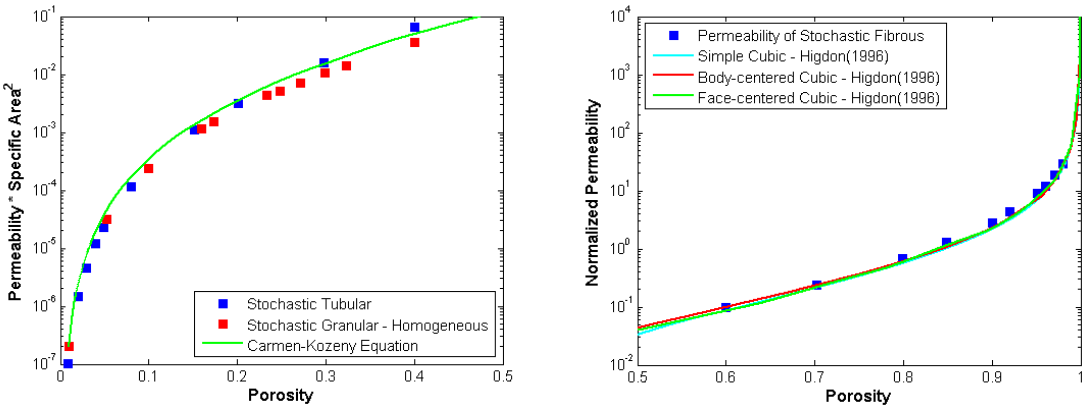

Figure 4-5: Porosity-permeability relation of idealized synthetic geometries established from single-phase lattice Boltzmann simulations.
Left: Geometries composed of interconnected tubes and those composed of fractures surrounding polyhedron grains; Right: Fibrous geometries. In both figures, the numerical results agree well with existing data / correlations.

To test the ability of the simulator to handle multiphase flows, a Shan-Chen two-fluid model [41, 42] was implemented, and some preliminary tests were conducted. The parameters in the Shan-Chen model are listed in Table 4-1.

Table 4-1: Parameters in the Shan-Chen model [3, 4] and their physical meanings.

$\sigma_{ij}\ (i \neq j)$	Interaction between fluid components i and j
σ_{ii}	Interaction between fluid component i and i (self interaction)
σ_{iw}	Interaction between fluid component i and solid wall
ρ_i	Density of fluid component i
τ_i	Relaxation parameter for fluid component i (controls viscosity)
M_i	Molecular weight of fluid component i
$\mathbf{g}_i$	Body force applied to fluid component i

Specifically, by adjusting σ_{ii}, σ_{ij}, and σ_{iw}, one can control the interfacial tension between fluid components i and j as well as the wetting characteristics of the solid wall with respect to the two fluids. Fig. 4-6 shows the formation of a spherical drop in an unbounded fluid and the equilibration of a drop on a solid wall. Fig. 4-7 shows the dependence of interfacial tension and contact angle on the model parameter σ_{12}.

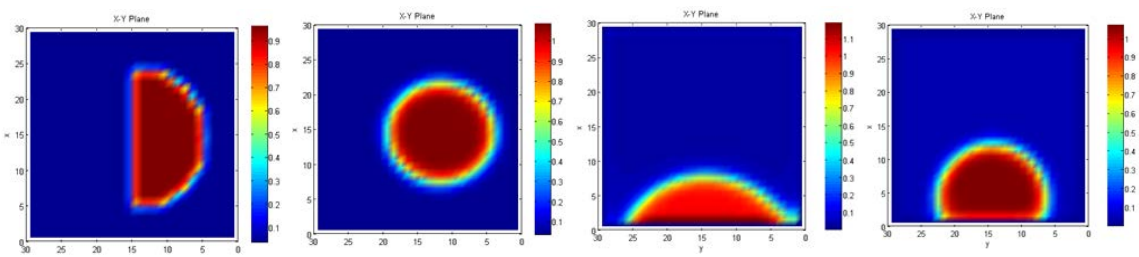

Figure 4-6: Two-fluid test conducted using the Shan-Chen model [9, 10].
From left to right: A droplet with a semi-spherical shape: (a) Is relaxed to a spherical shape; and (b) This process is used to extract the interfacial tension between the two fluids; c) An attractive interactive parameter set between the red fluid and the wall leads to a wetting contact angle; d) A repulsive interactive parameter set between the red fluid and the wall leads to a non-wetting contact angle.

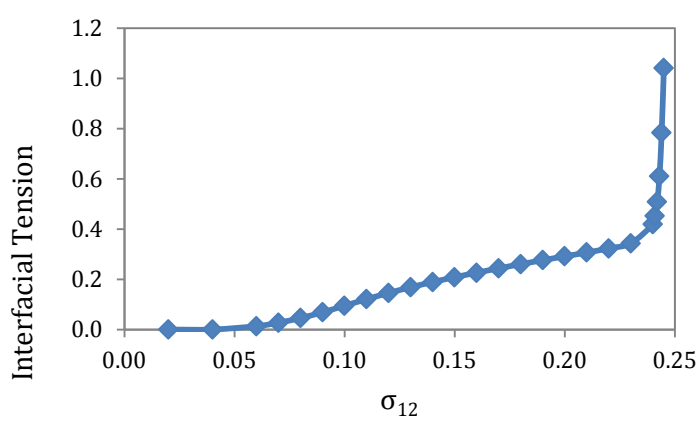

Figure 4-7: Dependence of interfacial tension, measured based on the pressure difference inside and outside a spherical drop, on the interaction parameter σ12.

4.4 Conclusions and Future Work

The objective of Task 7 was to develop a numerical capability to simulate a formation damage process and predict permeability reduction and fluid loss due to capillary trapping in low permeability formations. In the first year, significant progress has been made. A three-dimensional fluid flow simulator is developed. The simulator shows good parallel performance and predicts permeability accurately (single-phase flows). Preliminary results on two-phase flows show that the simulator can capture the physics of interfacial tension and wetting phenomena. In the second year, we will continue to run two-phase simulations in realistic geometries to predict permeability and fluid loss during invasion and flowback. In addition, we will develop a transport module for the simulator so that the role and fate of dissolved chemicals can be predicted.

5. Technology Transfer Efforts

5.1 Project Website

A project website has been created and is available at:
(http://web.mst.edu/~baib/Shale%20Gas/RPSEA_home.html)

It includes a research summary, capability, equipment, publications, and group members.

5.2 Presentations

Yin, X. "Numerical and Laboratory Study of Gas Flow through Unconventional Reservoir Rocks," oral presentation at RPSEA Piceance Basin Tight Gas Research Review meeting, April 21, 2011, Denver, Colorado, USA.

Elgmati, M., Zhang, H., Bai, B., Flori, R., and Qu, Q. Submicron-Pore Characterization of Shale Gas Plays. SPE 144050 presented at North American Unconventional Gas Conference and Exhibition. June 14, 2011, The Woodlands, Texas, USA, Society of Petroleum Engineers.

Elgmati, M., Zobaa, M., Zhang, H., Bai, B., and Oboh-Ikuenobe, F. Palynofacies Analysis and Submicron Pore Modeling of Shale-Gas Plays. SPE 144267 presented at North American Unconventional Gas Conference and Exhibition. June 14, 2011, The Woodlands, Texas, USA, Society of Petroleum Engineers.

Neeves, K. "Micro- and nanoscale porous media analogs for studying multiphase flow," invited presentation at the ORNL Center for Nanophase Materials Science User Meeting, September 9, 2011, Oak Ridge, TN.

Xiao, F., and Yin, X. "Porosity-Permeability Relations in Granular, Fibrous, and Tubular Geometries," oral presentation at American Physical Society, Division of Fluid Dynamics meeting, November 21, 2011, Baltimore, Maryland, USA.

5.3 Posters

Cheng, X., Wu, Q. Bai, B., Ma, Y. Velocity Profiling of polymer/aqueous phase interface in microchannel using single molecule imaging system, Poster at *Pittcon,* March 13, 2011, Atlanta, Georgia, USA.

5.4 Full papers

Elgmati, M., Zhang, H., Bai, B., Flori, R., and Qu, Q. (2011). Submicron-Pore Characterization of Shale Gas Plays. SPE 144050. North American Unconventional

Gas Conference and Exhibition. The Woodlands, Texas, USA, Society of Petroleum Engineers.

Elgmati, M., Zobaa, M., Zhang, H., Bai, B., and Oboh-Ikuenobe, F. (2011). Palynofacies Analysis and Submicron Pore Modeling of Shale-Gas Plays. SPE 144267. North American Unconventional Gas Conference and Exhibition. The Woodlands, Texas, USA, Society of Petroleum Engineers.

Wu, M., Xiao, F., Johnson-Paben, R., Retterer, S., Yin, X., Neeves, K. "Single- and Two-Phase Flow in Microfluidic Porous Media Analogs Based on Voronoi Tessellation," Lab Chip 12:253-261, 2012. The paper is featured on the cover of the journal.

REFERENCES

1. Wang, F., and Reed, R. Pore networks and fluid flow in gas shales. 2009.
2. Johnston, J., III, Heinrich, P., Lovelace, J., McCulloh, R., and Zimmerman. R. Stratigraphic Charts of Louisiana, L.G. Survey, Editor 2000: Folio.
3. Frantz, J.K., Jochen, V. Shale Gas White Paper, 2005, Schlumberger Marketing Communications.
4. Boughal, K. Unconventional plays grow in number after Barnett Shale blazed the way World Oil Magazine., 2008. 229(8).
5. Berman, A. The Haynesville Shale Sizzles with the Barnett Cools. World Oil Magazine., 2008. 229(9).
6. Sumi, L., Shale Gas: Focus on the Marcellus Shale, in Oil and Gas Accountability Project (OGAP)2008, Earthworksaction.
7. Navigant Consulting. "North American Natural Gas Supply Assessment," 2008, American Clean Skies Foundation.
8. U.S Dept. of Energy. Modern Shale Gas Development in the United States: A Primer, 2009, Ground Water Protection Council: Oklahoma City, OK.
9. Hillwood International Energy. Fayetteville Shale Power, 2007: Arkansas, USA.
10. Hayden, J., Pursell, D. The Barnett Shale, Visitors Guide to the Hottest Gas Play in the US, 2005, Pickering Energy Partners, Inc.
11. Sun, H., et al., A Nondamaging Friction Reducer for Slickwater Frac Applications, in SPE Hydraulic Fracturing Technology Conference2011: The Woodlands, Texas, USA.
12. Bragg, W.L. The Diffraction of Short Electromagnetic Waves by a Crystal. Proceedings of the Cambridge Philosophical Society, 1913. 17: p. 43-57.
13. Moore, D.M. and R.C. Reynolds, X-ray diffraction and the identification and analysis of clay minerals1997: Oxford University Press.
14. Austin, G.S. and K.E. Coose, Aggregate Reactivity and Concrete Durability in New Mexico. 1998.
15. Tiab, D. and Donaldson, E.C. Petrophysics: Theory and practice of measuring reservoir rock and fluid transport properties2011: Gulf professional publishing.
16. Yaalon, D.H. Mineral Composition of Average Shale. Clay Mineral Bulletin, 1962. 5(27): p. 31-36.
17. Biscaye, P.E. Mineralogy and sedimentation of recent deep-sea clay in the Atlantic Ocean and adjacent seas and oceans. Bulletin of the Geological Society of America, 1965. 76(7): p. 803.
18. Elgmati, M., et al. Palynofacies Analysis and Submicron Pore Modeling of Shale-Gas Plays. 2011.
19. Leverson, A.L. Geology of Petroleum, 2001 Edition, 1954, AAPG Foundation: Tulsa. p. 724.
20. Perrodon, A. Dynamics of Oil and Gas Accumulation. Elf Aquitaine, 1983: p. 366.
21. Kewen, L. and Abbas, F. Experimental study of wettability alteration to preferential gas-wetting in porous media and its effects. SPE Reservoir Evaluation & Engineering, 2000. 3(2): p. 139-149.

22. Osuji, C.E., Chenevert, M.E., and Sharma, M.M. Effect of Porosity and Permeability on the Membrane Efficiency of Shales, in SPE Annual Technical Conference and Exhibition 2008, Society of Petroleum Engineers: Denver, Colorado, USA.
23. Morini, G.L. International Journal of Thermal Sciences, 43 (2004) 631–651.
24. Hetsroni, G., Mosyak, A., Pogrebnyak, E., Yarin, L. International Journal of Heat and Mass Transfer, 48 (2005) 5580–5601.
25. Rostami, A.A., Mujumdar, A.S., Saniei, N. Heat and Mass Transfer, 38 (2002) 359–367.
26. Asako, Y., Nakayama, K., Shinozuka, T. International Journal of Heat and Mass Transfer, 48 (2005) 4985–4994.
27. Ewart, T. Perrier, P., Graur, I., Méolans, J.G. Journal of Fluid Mechanics, 584 (2007) 337–356.
28. Pitakarnnop, J., Varoutis, S., Valougeorgis, D., Geoffroy, S., Baldas, L., Colin, S. Microfluidics and Nanofluidics, 8 (2010) 57–72.
29. Morini, G.L., Yang, Y., Chalabi, H., Lorenzini, M. Experimental Thermal and Fluid Science, 35 (2011) 849–865.
30. Grega, L., and McGarry, M. (2007). Journal of Fuel Cell Science and Technology, Vol. 4 272-279.
31. Sugii, Y., and Okamoto K. (2006). Proceedings of ICNMM2006 96216.
32. Yoon, S.Y., Ross, J.W., Mench, M.M., Sharp, K.V. (2006). Journal of Power Sources. 160 1017-1025.
33. Voronoi, G., Angew, J.R. Math. 1908:97-178, 1908.
34. Okabe, A., Boots, B.N., Sugihara, K.O. Spatial Tessellations: Concepts and Applications of Voronoi Diagrams, Wiley, New York, 1992.
35. Thompson, K.E. AIChE J. 48:1369-1389, 2002.
36. Arns, C.H., Knackstedt, M.A., Mecke, K.R. Physics and Geometry of Spatially Complex Systems, in Morphology of Condensed Matter, K. R. Mecke and D. Stovan (Eds.), 33-74, 2002.
37. Lallemand, P., Luo, L.-S. Theory of the lattice Boltzmann method: Dispersion, dissipation, isotropy, Galilean invariance, and stability. Phys. Rev E 61: 6546, 2000.
38. d'Humieres, D. Multiple-relaxation-time lattice Boltzmann models in three dimensions. Phil. Trans. R. Soc. London A 360:437-451, 2002.
39. Yin, X., Xiao, F., Sundaresan, S. Permeability in fixed beds of spheres with size distributions and stochastically generated porous media analogs. Porous Media and Its Applications in Science, Engineering and Industry. AIP Conference Proceedings 124:15-20, 2010.
40. Wu, M., Xiao, F., Johnson-Paben, R., Retterer, S., Yin, X., Neeves, K.B. Single- and two-phase flow in microfluidic porous media analogs based on Voronoi tessellation, Lab Chip 12:253-261, 2012.
41. Shan, X., and Chen, H. Lattice Boltzmann model for simulating flows with multiple phases and components. Phys. Rev. E 47:1815-1819, 1993.
42. Kang, Q., Zhang, D., Chen, S. Displacement of a three-dimensional immiscible droplet in a duct. J. Fluid Mech 545:41-66, 2005.

LIST OF ACRONYMS AND ABBREVIATIONS

XRD: X-ray Diffraction
Bcf: billion cubic feet
Tcf: trillion cubic feet
EIA: US Energy Information Administration
USGS: United States Geological Survey
DIW: deionized water
TOC: Total organic carbon
SEM/FIB: Focused ion beam/scanning electron microscope